Phenomenological description of the effect of glass dissolution on cement paste evolution in an integrated glass dissolution experiment

Jules Goethals, Karine Ferrand, Régine Mosser-Ruck, Julien Bonnet, Karine David, Sanheng Liu, Jérôme Sterpenich, Abdesselam Abdelouas, Yann Morizet, Karel Lemmens

Phenomenological description of the effect of glass dissolution on cement paste evolution in an integrated glass dissolution experiment.

J.Goethals[a], K.Ferrand[b] , R. Mosser-Ruck[c], J. Bonnet[c], K. David[a], S. Liu[b], J. Sterpenich[c], A. Abdelouas[a], Y. Morizet[d], and K. Lemmens[b]

[a] *Laboratoire Subatech, UMR 6457, 4 rue Alfred Kastler, La Chantrerie CS 20722, 44307 Nantes CEDEX 3*

[b] *SCK-CEN, Belgian Nuclear Research Centre, Boeretang 200 - BE-2400 Mol, Belgium*

[c] *GeoRessources, UMR 7359, CNRS-INSU-Université de Lorraine-CREGU, Faculté des Sciences, Campus Aiguillettes, BP 70239, 54506 Vandœuvre-lès-Nancy, France*

[d] *Laboratoire de Planétologie et de Géosciences (LPG) UMR 6112, 2 rue de la Houssinière - BP 92208 44322 Nantes Cedex 3, France*

Abstract

The interaction between nuclear glass surrogate and ordinary Portland cement (OPC) was investigated through integrated static leach tests conducted at ambient temperature. Tests were performed in stainless-steel cells in which OPC hydrated pastes were separated from glass powders by a stainless-steel filter. This article gives a phenomenological description of the processes affecting the hydrated cement paste arising from glass dissolution. The results show that the ingress of Si from glass dissolution leads to the degradation of the cement paste over a distance of 100 – 200 µm within 900 days of interaction. The Hardened Cement Paste (HCP) is affected by two main processes, which are the pozzolanic reaction and the alkali-silica reaction (ASR). These processes lead to porosity changes of HCP at contact with the stainless-steel filter and significant changes in the diffusive properties of the HCP. Especially, the effect of such processes on boron and lithium retention was studied and showed that precipitation of ASR-like gel and low Ca/Si C-S-H (Calcium Silicate Hydrate) highly retain these two elements. In the presence of an Al-rich glass (SM539), ASR is unlikely due to the preferential formation of C-A-S-H (Calcium Aluminium Silicate Hydrate).

Keywords: integrated tests, glass dissolution, cement degradation, ASR (alkali-silica reaction), pozzolanic reaction.

1 Introduction

In many countries, high and intermediate-level reprocessing wastes are immobilized in borosilicate glass (e.g., France, Switzerland, Belgium,Netherlands). In the vitrification process, the molten glass is poured into a stainless-steel cask, itself emplaced in a steel overpack. Together, these elements constitute the waste package. The waste packages will be surrounded by engineered barriers and emplaced within a host rock. In the concepts of Belgium (Gens et al., 2006; Wickham et al., 2005) and the Netherlands (Verhoef et al., 2017), the Boom Clay formation is a potential host rock. . Typically, the Belgian and Dutch concepts rely on the supercontainer design where large amount of cementitious materials are involved in the vicinity of the waste packages. After the failure or perforation of the stainless-steel cask and the carbon steel overpack, there will be an ingress of water from the Boom Clay. The incoming Boom Clay porewater will be conditioned by the percolation through the cementitious materials. With high pH cement such as OPC, porewater can potentially become very alkaline (pH≈ 13.5). Thus, some studies were devoted to the alteration of glass in alkaline (Gin and Mestre, 2001; Ribet and Gin, 2004) to hyperalkaline solutions (Depierre, 2012; Elia et al., 2016; Ferrand et al., 2022, 2021; Mann et al., 2019), and others to glass alteration in hyperalkaline solutions and with the presence of cementitious materials (Andriambololona et al., 1991; Ferrand et al., 2013; Suzuki-Muresan et al., 2018). In these latter studies, the authors reported that cementitious material triggers glass alteration because Si and Al dissolved from the glass can react with portlandite from the cement, to form C-S-H and/or C-A-S-H (Ferrand et al., 2013; Liu et al., 2015). To study the dissolution behaviour of reference waste glasses in the proximity of a high pH cement, integrated experiments were performed at SCK-CEN as part of the programme of ONDRAF/NIRAS on the geological disposal of high-level/long-lived radioactive waste. Lab-scale mock-ups of the waste package and near-field barriers were developed, including a layer of glass powder, a stainless-steel filter, and an ordinary Portland hydrated cement paste layer. Glass powders, rather than glass monoliths, were used, to increase the reactive glass surface area, which was supposed to lead to a more pronounced alteration of the hydrated cement paste. The stainless-steel filter was added to simulate the perforated stainless-steel cask and carbon-steel overpack separating the glass from the cementitious material. The experiments were conducted at approximately 20°C, which is the expected temperature in the Dutch and Belgian disposal geological repositories (DGR), few decades after disclosure (Kursten and Druyts, 2015; Verhoef et al., 2017). It should be noticed that such set-up mimics the real repository conditions to a limited extent due to the high reactive surface of glass employed in order to accelerate the cement degradation processes. As a result of the interaction between the glass and the HCP, processes take place both on the glass surface and in the

neighbouring HCP. For performance assessments of the disposal system, it is also important to investigate the evolution of the transport properties of the cementitious material, especially for the modelling of radionuclides migration in this evolving material. Indeed, the HCP will degrade with time due to its reactions with the glass on one side of the system and with the Boom clay porewater on the other side (pH of 8.3-8.6 (De Craen, 2006)). At both interfaces, the cementitious material will react with the surrounding material and evolve with time. Its porewater will evolve with the mineralogical changes. Such evolution is very slow and is generally described as the succession of three stages (Atkinson et al., 1987; Wang, 2009), which are:

Stage 1: young concrete water (YCWCa); this water is enriched in alkalis and has a high pH value of around 13.5.

Stage 2: evolved concrete water; after leaching out of dissolved alkalis, this water has a pH value of 12.5 controlled by the dissolution of portlandite.

Stage 3: C-S-H concrete water; portlandite dissolves away completely, decalcification of C-S-H occurs and pH drops below 12.

Moreover, two main processes may occur at the interface between glass and cement. The first one is the pozzolanic reaction, which consists in the reaction of portlandite with dissolved silica to form low Ca/Si C-S-H (Dodson, 1990). The second one is the alkali-silica reaction, which involve a source of reactive silica, alkalis and water (Dent Glasser and Kataoka, 1981; Rajabipour et al., 2015).
The integrated static leach tests presented in this paper are of particular interest to study these processes and to assess their extent in a relatively short period of time. A set of characterization techniques [Scanning Electron Microscopy coupled with Energy Dispersive X-ray analyses (SEM-EDX), X-ray diffraction (XRD), Thermo-gravimetric analyses (TGA), Laser ablation induced coupled plasma-mass-spectrometry (LA-ICP-MS), µ-Raman spectrocopy] was employed to assess the chemical, mineralogical and microstructural evolution of HCP after 900 days of interaction with glass and young cement porewater. These characterizations allowed a better comprehension of the mechanisms involved at the reaction front between glass and HCP. The experimental findings of this study fairly agree with the geochemical modelling results given in a companion paper (Liu et al., 2024, submitted) and the relevant processes occurring at such interfaces can be further considered in large scale geochemical models.

2 Materials and Methods

2.1 Materials and porewater chemistry

2.1.1 Glasses

The widely employed SON68 glass, which is an inactive surrogate of the R7T7 French radioactive glass and the Al-rich SM539 HE 540-12 surrogate glass (Belgian reference Pamela glass) were selected for the integrated tests. The first one was selected due to the broad knowledge on its alteration behaviour in different media and the second was selected because it was more representative of the Belgian concept. SON68 glass rods with a density of 2.75 ± 0.01 g/cm^3 were provided by the French Alternative Energy and Atomic Energy Commission (CEA). SM539 glass with a density of 2.45 ± 0.01 g/cm^3 was synthesized at SCK-CEN. It was prepared in-house by mixing the appropriate oxides and hydroxides in a platinum crucible at 1150 °C for approximatively four hours. Then, the melting glass was cooled down to room temperature at a rate of about 50 °K per hour. The theoretical chemical compositions of these glasses are given in Table 1. The glass rods were crushed, sieved to a size fraction between 125 and 250 µm and cleaned ultrasonically in deionized water. The specific surface area measured by BET (Brunauer, Emett and Teller) using Kr adsorbent gas equals 0.0310 ± 0.0002 m²/g for both glasses.

2.1.2 Hardened ordinary Portland Cement Paste

The selected ordinary Portland cement (OPC) was the CEM I42.5 R HSR LA Portland cement provided by CIBELCOR®, which composition is given in Table 2. In order to perform the integrated tests, hardened cement paste (HCP) was prepared at room temperature (approximately 20°C) by adding 3000 g of OPC in a mixer filled with 1200 g of tap water (water to cement ratio (W/C) = 0.4). Another batch of HCP with a similar W/C was produced from the same OPC batch to analyse the pristine composition of HCP (section 3.1.1).

2.1.3 Porewater chemistry

Cementitious water at pH $_{(25\,°C)}$ 13.7 ± 0.2 referred to as Young Cement Water with Calcium (YCWCa), which simulates the porewater in equilibrium with HCP at the first stage of degradation was synthesized by dissolving appropriate amounts of $Ca(OH)_2$, KOH, NaOH, Na_2SO_4, and $CaCO_3$ in High Performance Liquid Chromatography (HPLC) degassed water (Ferrand et al., 2018). This cement water was prepared in a glove box under Ar atmosphere to prevent any carbonation and was stored in a polyethylene bottle. After two months, pH and elemental concentrations were measured to check if the target pH and composition determined from geochemical modelling were reached. The measured composition of the porewater is given in Table 3.

2.2 Experimental set-up

The integrated tests were performed at room temperature (approximately 20°C) in a stainless-steel cell (length = 135 mm; internal diameter = 80 mm), which was filled with HCP and a layer of glass powder (SON68 or SM539 with a size fraction between 125 and 250 µm) separated by a 2.5 mm thick stainless-steel filter (316L from GKN®) with a 10 µm average pore diameter. After mixing, the hydrated cement paste was poured into the stainless-steel cells, stirred with a spoon and let to harden for 20 days. Then, four holes were drilled in the cement plugs (diameter = 6 mm, height = 75 mm, V= 2.12 mL), whereas in the glass compartments a tubular stainless-steel filter (V = 5.63 mL, 110 µm average pore diameter) was placed for solution sampling. The drilled sampling holes were filled with the synthetic cementitious solution (YCWCa) and an increasing Ar pressure from 2 to 15 bar was applied to accelerate the saturation of the cement plug without introducing CO_2 in the system. The holes were regularly checked and refilled when they were empty. After 1 year, the cell reached a constant weight after addition of a cumulated total volume of approximately 45 mL of YCWCa. When the volume of the glass compartment was completely filled with YCWCa, as indicated by the filling of the tubular filters, Ar pressure application was stopped to let the system under static conditions. Then, the tests were running for 900 days in fully saturated conditions. After this period, porewater was progressively vapored due to the imperfect sealing of the cell and also consumed by cement hydration without further refilling of the tubular filters during 1530 days more. Finally, the cells were dismantled. It should be noticed that very limited interactions are considered during the period of unsaturated conditions. More details on sampling and refilling of the cells until dismantling are given in Table. S1. A cross section of the cell is presented in Fig. 1.

2.3 Solution analyses

Aliquot solutions of 1 mL were regularly taken from each hole for pH and solution analyses.
The pH was measured using a Mettler Toledo micro-electrode (Inlab® Micro) calibrated with HANNA buffers at pH 7 and 13. A verification of the calibration was done with HANNA buffers at pH 10 and 12, respectively. The uncertainty (95% confidence interval) on a high pH measurement is lower than 0.2.
For solution analyses, the aliquot solutions were diluted with ultrapure water (18.2 Ω.cm) and ultrafiltered at 10,000 D. Then, the samples were acidified with ultrapure HNO_3 (67 – 69%) and analysed to determine Al, B, Ca, Fe, K, Si, Li, Mg, Mo, Na, Sr, Cs concentrations by Inductively Coupled Plasma-Atomic Emission Spectroscopy (ICP-AES) or Inductively Coupled Plasma-Mass Spectrometry

(ICP-MS) and Cl^-, SO_4^{2-} concentrations by Ionic chromatography (IC). For both analytical techniques, the uncertainty (95% confidence interval) was equal to 10%.

It should be noticed that sampling was not possible in some of the drilled holes after 18 months. Each hole was thus refilled with YCWCa containing an adjusted silicon concentration similar as the one sampled at 12 months (Table. S2). These solutions were prepared from Si ICP-MS standard solution (10 g/L) and YCWCa in appropriate amounts.

2.4 Sample preparation for solid characterizations

The tests were dismantled 1530 days after the last sampling, i.e., after a total duration of 2430 days. In a first instance, the solution was removed from the cells by applying Ar pressure until a constant weight was reached, then a lyophilisation was done and the whole system was embedded under vacuum in an epoxy resin. Note that during this operation, the resin did not penetrate into the cement paste due to its too low porosity. The embedded glass/stainless-steel filter/HCP assembly was first collected by drilling cores (3 cm diameter) in the cells (Fig. S1a). The cores were then cut into two with a diamond saw, embedded into epoxy resin and polished using abrasive SiC disks (600, 800, 1200, 2400, 4000) and diamond paste (1 µm) prior to their characterization (Fig. S1b). These samples were used for µ-Raman spectroscopy and LA-ICP-MS measurements and previously carbon coated for SEM-EDX measurements. The rest of the cell contents were obtained after pickling the stainless-steel cells with a lathe milling machine (Fig. S1c). During this latter operation, the exposed surfaces (top and bottom of the cells) were protected with silicone paste to avoid contamination from water cooling fluid used for cutting. The interfaces between the different materials were totally preserved during this process. The content of the cells was first embedded into epoxy resin and prepared for XRD, TGA, LA-ICP-MS and water porosity measurements. All the cutting and polishing operations were realized with ethanol or without any lubricating fluid to preserve the samples from carbonation and other alteration processes.

2.5 Solid characterization methods

2.5.1 Scanning Electron Microscopy coupled with Energy Dispersive X-ray spectroscopy (SEM-EDX)

SEM images in backscattered electron (BE) mode and EDX analyses and mappings were collected with a TESCAN VEGA3 with a counting time of 60 s, 20 kV, 1.5 nA for EDX analyses and 1 ms per pixel, 15 kV and 1 nA for mappings. The interaction pear of the X-ray beam with the hydrated cement paste

was limited to few (μm^3) which still implied overlapping of contributions of several nanometric phases in the cement matrix. BE-SEM images were also collected with a JEOL 7600F microscope operating at 15 KV and 0.5 nA at IMN (Institut des Matériaux de Nantes) for phase quantification by grey level analyses. These latter were assessed at the interface between HCPs and the stainless-steel filters using Jmicrovision© (Roduit, 2007). Images were collected at different magnifications (x500, x800, x1000, x1500), adapted to the analysed area. The total covered surface area was chosen high enough to be representative of the cement paste heterogeneity. The images contain pixels with different shades of grey ranging from 0 (black) to 255 (white), which are linked to the contrast of the phase and its BE (backscattered electron) coefficient η. The fractional volume of a phase is proportional to its image area (Scrivener, 2004) and was determined by integrating the histogram in the interval of grey level corresponding to a phase or a group of phases. For that purpose, the nature of the different phases or group of phases were previously determined with EDX hyperspectral mapping. With this method, it was possible to distinguish C_4AF, C_2S/C_3S together and newly precipitated C-(A)-S-H from the other components of the hydrated cement paste. As in the study of (Hu and Ma, 2016), the porosity was segmented into porosity (here denoted as coarse porosity) and very porous products. The grey level boundaries were adjusted manually in the histograms to fit the BE-SEM images. The Fig.S2 shows examples of grey level boundary adjustments for altered and unaltered region of HCP for both cells and reports the total surface analysed for each area of interest.

2.5.2 X-ray diffraction (XRD)

After the dismantling of the cells, cement paste slices were cut with a diamond wire saw in order to preserve the interface, and the slices were directly scanned in a Bragg-Brentano geometry both at the interface and approximately 2 mm further in the HCP. The stainless-steel filter pieces coming from the cells were taken off and analysed in the same geometry. A D5000 Bruker AXS diffractometer equipped with a Cu anticathode (λ = 1.5406 Å) operating at 40 kV and 25 mA was used. The scans were collected with a LINXEYE 1D detector using an anti-air-scatter in the range 2θ = 5° to 70° with a step size of 0.01° and 3 sec/step. The divergence slits were fixed to 0.28 mm and the K-Beta ray was filtered using a Ni filter.

2.5.3 Thermo Gravimetric (TG) analyses

The TG analyses were carried out using a Setaram TG-DSC 111 thermo-gravimetric analyser. Approximately 16 mg of ground powders, dried under Ar with silica gel for at least 24 hours, were

placed in a Pt-Rh crucible and heated to 1000°C under a nitrogen flow of 70 ml/min at a rate of 10°K/min. Blank measurements were subtracted from the scans to correct for the buoyancy effect. The analyses were conducted in duplicate in order to assess the standard deviation of the results.

2.5.4 µ-Raman spectroscopy (µ-RS)

The µ-Raman measurements were acquired using a Jobin-Yvon Labram© HR800 Evolution spectrometer equipped with a 1200 lines/mm grating. The Raman excitation was applied using a solid-state 633 nm wavelength laser set at low power (<1 mW) to avoid phase degradation under the beam. The laser beam was focussed using a 100× Olympus objective leading to a theoretical spot size of 0.90 µm. The acquisition time on a given sample was typically between 20 and 60 s and 10 accumulations. Calibration on a silicon standard using the 520.5 cm^{-1} band was performed prior to measurements. The spectra were acquired using the Labspec 6 © software package, and when possible, the RRUFF database (Lafuente B, Downs R T, Yang H, 2015) was used for phase identification.

2.5.5 Laser Ablation – Induced Coupled Plasma – Mass Spectrometry (LA-ICP-MS)

LA-ICP-MS profiles of 58 elements were collected across the HCP, in order to assess: (i) the chemical changes occurring between HCP and glass (separated by a stainless-steel filter) and (ii) the diffusion of glass dissolution tracer elements across the HCP. Indeed, an increasing interest was devoted to this technique for cementitious material characterization as it allows a high spatial resolution along with multi-element analyses (Decker et al., 2021). As the HCP is a heterogeneous multiphase matrix, the line ablation mode was chosen to obtain mean profiles for each measured element. Generally, calcium is used as internal standard (Bonta et al., 2016; Gastel et al., 1997), provided that this element is not varying in the HCP due to degradation processes. As the concentration of major elements (e.g., Ca, Si, Al) was susceptible to vary at the interface, the sum normalization process was used to calculate the concentrations of the 58 elements measured (Gagnon et al., 2008; van Elteren et al., 2009). The detailed sample acquisition parameters are reported in Table. S3. Both NIST 1881b and NIST 610 were used as internal standards for major elements and NIST 610 was used for glass dissolution tracers. The NIST 1881b was prepared in an Ar filled glove box by mixing milli-Q® water with NIST 1881b cement powder with a W/C ratio of 0.42. The HCP cylinder was let to harden for 28 days and dried in a glove box prior to its embedding in epoxy resin and polishing down to 1 µm with diamond paste.

3 Results

3.1 Mineralogical, chemical and microstructural evolution of the HCP

3.1.1 The pristine HCP

In a first instance, solid characterizations were conducted on a pristine CEM I 42.5 HSR LA cement paste cured for 20 days. The diffraction pattern of this HCP is presented in Fig. S3. It reveals the presence of (hkl) reflections corresponding to portlandite (CH), brownmillerite (C_4AF), alite (C_3S), belite (C_2S), ettringite ($C_6A\bar{S}_3H_{32}$), calcite ($C\bar{C}$), monocarboaluminate ($C_4A\bar{C}H_{11}$), hemicarboaluminate ($C_4A\bar{C}_{0.5}H_{12}$) and periclase (M) . The HCP also contains C-S-H detected by the presence of a bulge near 2θ = 30°. The portlandite (18.5 (±2.1) vol.%) and calcite (1.3 (±0.2) vol%) contents of this HCP were estimated from TG analyses and the C_2S/C_3S (11.7 (±2.8) vol%) and C_4AF (3.4 (±0.7) vol%) contents were assessed by means of SEM grey level analyses. The porosity of this HCP was also assessed by water porosity measurement following a modified current standard (NF P18-459) used in France (e.g., (Lalan, 2016)) with a drying temperature of 60°C to limit hydrates degradation. A porosity of 36.6 (± 1.4) vol% was determined from measurements on four samples.

3.1.2 Mineralogical and microstructural evolution of the interface

Mineralogical and microstructural changes of the HCP at the interface with the stainless-steel filter were assessed by means of SEM-EDX, XRD, and µ-Raman. The Fig. 2 and Fig. 3 show annotated SEM pictures of the HCP along with EDX mappings for SON68 and SM539 cells, respectively.

3.1.2.1 The unaltered HCP

For both cells, a heterogeneous altered layer is present at the interface between HCP and the stainless-steel filter. Below these altered layers, the cement paste seems unaffected by alteration. This area will be further denoted as A0 in the manuscript. In this area, the BSE mode imaging and the EDX analyses reveal the presence of unhydrated cement clinkers (UC) such as brownmillerite (C_4AF), belite (C_2S) and alite (C_3S). The amount of UC is higher in the SM539 cell. This difference is probably to link with the experimental method. Indeed, the cement paste for the two cells was prepared in a similar container and poured in the SON68 cell first and then, in the SM539 cell. Even though the water-cement mixture was stirred in the container, gravimetric segregation may have occurred, leading to such difference for the two cells. The matrix surrounding the UC grains consists in hydrated cement paste principally composed of a mixture of C-S-H and portlandite. This latter phase

is also present as large platy crystals in the unaltered HCP. Some S-rich phase and/or group of phases (probably mostly AFt) are also evidenced by EDX mappings (Fig. S4). These phases are present as needle crystals filling the porous areas. These porous areas are also sometimes filled by spherules rich in Ca and O typical of calcite. Eventually, some large grains containing Mg and O (probably periclase) are also present, dispersed in the unaltered HCP (Fig .S4). In order to complete these observations, XRD analyses were conducted at 2 mm from the interfaces (Fig. 4). In addition to the phases revealed by SEM-EDX analyses, hemicarboaluminate, monocarboaluminate and hydrogarnet with the following composition $Ca_3(Al_{1-x}Fe^{3+}_x)(SiO_4)_{3-y}(OH)_{4y}$ are identified in the unaltered HCP. The occurrence of this latter phase is scarce in cementitious material and this phase is observed in this cement paste due to the high amount of C_4AF vs C_3A in the clinker employed for this study (Lalan et al., 2016). However, the exact composition of this phase couldn't be defined by XRD. The TG measurements on the sample collected in the same region of the HCP allow quantifying the portlandite content in the unaltered HCP and reveal the presence of two different types of carbonates as indicated by the presence of a double peak in the first derivative of the TG signal between 680 and 800°C (Fig. S5). The temperature decomposition of carbonates highly depends on the fineness of the carbonate phase. The two bulge observed are typical of the presence of carbonates in the original clinker associated with the presence of mono- or hemicarbo(alumi)nates and possibly carbonation of portlandite and C-S-H (Lothenbach et al., 2016) . As for the pristine HCP cured for 20 days, the porosity of the unaltered HCP was assessed by water porosity measurement on samples free of fractures, collected at great distance from the interface (>1cm). Open porosity of 21.3 (± 2.4) and 25.9 (±0.3) vol% are obtained on three samples for the HCP coming from SON68 and SM539 cells, respectively. These quite low values can be explained by the long-time of hydration of the HCP and its carbonation that may have occurred after dismantling.

Compared to the freshly prepared cement, the largest differences are the more advanced state of hydration, the carbonation of the HCP and the decrease of the porosity.

3.1.2.2 Altered HCP and phase precipitation

Mineralogical and microstructural changes occurred in four distinct areas for both cells. Starting from the HCP compartment to the glass compartment, these zones correspond to altered HCP (A1), secondary alteration products (S.A.P.) edging the HCP (A2), S.A.P. in the filters close to the HCP compartment (A3) and S.A.P. in the filter close to the glass compartment (A4). These areas are separately described in the next paragraphs.

The altered HCP (A1) is characterized by an increase of the coarse porosity (i.e., the porosity filled by epoxy resin after sample preparation that can be probed by SEM) over a distance of approximately 200 µm and 100 µm for the SON68 and SM539 cells, respectively. However, this porosity is partly

filled by a Ca - Si gel, containing Al in the SM539 cell. This gel is less dense than the initial hydrates and made of sub-micrometric fibers containing clusters, as can be seen in Fig. 2-c. Such phase arrangement create a nanometric porosity network that is referred as gel porosity hereafter. In the SON68 cell, the Ca/(Si+Al) ratio of this gel is around 1.3 indicating that this gel can correspond to a low Ca/Si C-S-H phase (Fig. 5). In the SM539 cell, the Ca/(Si+Al) ratio of this gel increases with distance from the stainless-steel filter from about 0.4 to 0.85 (Fig. 5). In parallel, the Al/Si ratio of this gel decreases with distance from the stainless-steel filter. In this cell, this gel is also filling cracks, which were probably formed during the curing of the HCP in the vicinity of the interface (Fig. 3). The nature of the gel that precipitated in the SM539 cell seems to be more complex than in the SON68 cell due to its chemical heterogeneity. However, it can be considered as a low Ca/Si C-A-S-H phase more or less enriched in Al and Si. Moreover, Na and K enrichments are depicted in the Ca – Si-(Al) gel in both cells, indicating a significant alkali uptake in it (Fig. 2,3 and 5). The altered area also still contains a small amount of UC phases such as C_4AF and C_2S/C_3S. However, the C_2S and C_3S grains are partially or totally replaced by inner HP (hydration products) in this area, with a more pronounced hydration of UC in the SON68 cell (Fig. 2 and Fig. 3). The XRD analyses conducted on the samples collected at the interface between stainless-steel filter and HCP mostly revealed the presence of calcite for both cells, indicating that carbonation occurred in this area (Fig. 4). Moreover, the intensity of (hkl) reflections associated to portlandite and ettringite drastically dropped for both cells signifying that these phases were at least partially depleted in the altered layer.

In addition to this interface degradation phenomenon, S.A.P. were observed both edging the HCP (A2) and precipitating in the stainless-steel filter pores (A3).

In the SON68 cell, these S.A.P. have a low Ca/Si ratio of ≈ 0.7 in the stainless-steel filter, and of ≈ 0.5 - 0.6 edging the HCP (Fig. 5). In both cases, these S.A.P. are highly enriched in alkalis (Fig. 2 and 5). The thickness of the S.A.P. edging the HCP is heterogeneous reaching up to 160 µm and with a mean thickness of 30-40 µm. These S.A.P. are dense and form a crust over the altered area with a very low porosity. In an attempt to characterize this phase more thoroughly, µ-Raman analyses were conducted on the S.A.P. edging the HCP (Fig. 6a). The spectra collected for these precipitates present similarities with C-S-H Raman signal. The broad bands centred around 650 cm^{-1}, with a shoulder at approximately 600 cm^{-1} and the band at approximately 1065 cm^{-1} can correspond to the bending vibration of Si-O-Si linkages and to the Si-O stretching vibrational modes both present in C-S-H (Kirkpatrick et al., 1997). The large broadening of these bands indicates that this phase is poorly crystalline or amorphous. Indeed, these phases were not observed in the diffraction pattern collected at the interface. Those spectra also present similarities with amorphous gel that precipitates during ASR (alkali-silica reaction), with Ca/Si ratio of 0.33 and (Na+K)/Si ratio of 0.36 (Leemann et al., 2020). Indeed, the broad band centred near 650 cm^{-1}, with the shoulder around 600

362 cm^{-1}, can correspond to Q^2 and Q^3 sites bending vibrations respectively, and the band centred around
363 1065 cm^{-1} can correspond to a combination of stretching vibration arising from Q^2 and Q^3 sites
364 (Balachandran et al., 2017; Leemann et al., 2020). The sharp band located near 1080 cm^{-1} can be
365 attributed to partial carbonation of this phase or to the presence of calcium carbonates in the S.A.P.
366 layer. Thus, this S.A.P. layer might be a mixture of ASR-like gel and calcium carbonates, explaining the
367 high Ca/Si ratio for such ASR-like gel.
368 Locally in the S.A.P. layer edging the HCP, µ-Raman evidenced the presence of monocarboaluminate
369 ($Ca_4Al_2CO_9$. $11H_2O$) in the SON68 cell (Fig. 6 b), with the presence of bands centred at 529 cm^{-1} and
370 1067 cm^{-1} corresponding to the stretching vibration of the $Al(OH)_6$ octahedral groups and to the
371 stretching vibration of the CO_3^{2-} groups, respectively (Torréns-Martín et al., 2013).

372 In the SM539 cell, these S.A.P. have low Ca/(Si+Al) ratio of ≈ 0.4-0.6 in the filter close to HCP and of ≈
373 0.25-0.35 in the layer edging the HCP. These phases are also highly enriched in alkalis with
374 (K+Na)/(Si+Al) ratio between 0.2 and 0.4. The layer that precipitated close to the HCP is relatively
375 thin (5 to 10 µm) compared to the one observed in the SON68 cell and is also forming a dense crust
376 over the altered area. It has a layered structure (Fig. 3 b) with sub-layers more or less enriched in Si.
377 As this edging S.A.P. phase is quite complex, and as the spatial resolution of µ-Raman was not
378 sufficient to analyse it layer by layer, it is difficult to interpret the Raman signal arising from its
379 analysis (Fig. 6 c). Like for the S.A.P. observed in the SON68 cell, the broad bands centred around 675
380 cm^{-1} and 1080 cm^{-1} can again correspond to the bending vibration of Si-O-Si linkages and to the Si-O
381 stretching vibrational modes in C-(A)-S-H, or to the Q^2 and Q^3 sites symmetric stretching and bending
382 vibrational modes observed in ASR gel. The sharp band located near 1080 cm^{-1} is again due to the
383 partial carbonation of this phase. The broad bands can be shifted compared to the ones observed in
384 the SON68 cell due to the incorporation of aluminium in this phase (Ortaboy et al., 2017). However, a
385 large background signal is depicted in the spectra collected on this phase. This background signal can
386 be linked to the presence of a glassy phase mainly composed of Si and alkalis coexisting with the C-A-
387 S-H phase or the ASR gel.

388 The precipitates observed in the stainless-steel filter close to the glass compartment (A4) have a
389 quite similar composition in SON68 and SM539 cells with Ca/Si ratio of 0.03 and 0.02, Al/Si ratio of
390 0.38 and 0.47 and (K+Na)/(Si+Al) ratio of 0.45 and 0.27 (Fig. 5). Those precipitates have a
391 composition similar to K-phillipsite, a mineral that belongs to the zeolite group. The XRD analyses
392 conducted at the surface of the stainless-steel filter surfaces showed that these phases were
393 amorphous or poorly crystallized (Fig. S6).

394 ### 3.1.3 Chemical profiles in the HCP
395

Compositional profiles of the oxides of major constituting elements from the HCP were acquired by LA-ICP-MS (Fig. 7). As the HCP is a heterogeneous multiphase matrix, the line ablation mode was chosen to obtain mean profiles for each measured element. In both cells, chemical changes in the major HCP constituents are observed in the first 300 µm. At further distance from the interface, the oxide contents in the unaltered HCP are very close to those of the initial clinker. Indeed, these measurements excluded all the H_2O and CO_2 content volatilized during ablation of the HCP that were not measured in our conditions and the profiles were not corrected from loss on ignition measurements.

One major change observed at the interface is the strong depletion of sulphate up to approximately 300 µm for both cells. This decrease in the sulfate content is associated with a dissolution of ettringite and maybe amorphous monosulfoaluminate over a distance of 300 µm in the HCP. Moreover, the interfaces are characterized by an increase in the alkali content, already depicted by SEM. In the SON68 cell, the first line analysed (approximately between 0 and 50 µm from the interface) is highly enriched in K and Na. This increase is associated with a strong decrease in the Ca/Si ratio, in agreement with the presence of an ASR-like gel edging the HCP. In the SM539 containing phase, the alkalis diffused over up to 300 µm in the HCP. However, in this cell, the Ca/Si ratio is constant over the whole profile. This is to link with the lower Si influx from the SM539 glass compartment compared to the SON68 one (Table S4). The concentrations of Al and Fe, slightly decrease at the interface in the SON68 cell and their concentration is strongly correlated in the profile. Indeed, these two elements are generally associated with the same cementitious phases (i.e., in C_4AF, hydrogarnet, ettringite). However, the decrease in the Al content is not correlated with the sulphate decrease, meaning that dissolution of ettringite at the interface implies the formation of another Al-containing phase such as monocarboaluminate or C-A-S-H.

3.1.4 Determination of the mineralogical evolution of the HCP

In order to further compare the extent of the degradation front in the HCP with the geochemical model presented in the companion paper (Liu et al., 2024, submitted), a quantitative assessment of the mineralogical changes in the cement compartment was estimated from the solid characterizations combined with the chemical profiles. This assessment is based on the following simplifications:

(a) Among the three types of nanocrystalline C-S-H available in the Thermochimie database version 11 a (Blanc et al., 2015) which are C-S-H 0.83, C-S-H 1.2 and C-S-H 1.6, only two were predicted by the model for both cells (C-S-H 1.2 and C-S-H 1.6). Thus, only these two types of C-S-H were

considered in the assessment of the mineralogical profiles. Regarding the Ca/Si ratio of the newly formed phase in the altered area of the SON68 cell, the choice of C-S-H 1.2 agrees well with experimental data (Fig. 5). In the SM539 cell, the use of C-S-H 1.2 is less obvious because of the heterogeneous Ca/Si ratio obtained for the corresponding phase. Still, as the Si/Al and Ca/Si ratios of this phase increase with distance from the stainless-steel filter, the choice of C-S-H 1.2 is consistent.

(b) The decalcification of C-S-H 1.6 in the altered area where portlandite is depleted is considered for both cells, even though there is no direct experimental evidence of this phenomenon. The latter hypothesis is based on direct experimental observation in previous studies where cementitious material were placed in contact with Si rich media (e.g.,(Dauzeres et al., 2010)).

(c) The Si-hydrogarnet composition is fixed and corresponds to the composition experimentally determined in an old hydrated OPC (Dilnesa et al., 2014).

(d) The Mg is entirely incorporated in periclase even if brucite and hydrotalcite can be present in the cement paste and that anhydrous phase such as C_3S and C_2S can also contain a small fraction of Mg (Gharibi et al., 2017). However, hydrotalcite is generally present only in very low amount in hydrated OPC paste without Mg-bearing additives (e.g.,(Machner et al., 2018)).Due to the low amount of magnesium in the cement paste, this approximation has only a slight effect on the mineralogical and microstructural profile determination.

(e) All the sulphur content is considered to be incorporated in ettringite even though monosulfoaluminate can coexist with this phase.

(f) The C_2S/C_3S, C_4AF contents were determined by SEM grey level analyses in two areas (i.e., altered and unaltered areas) and were thus fixed, using a Ca/Si ratio of 2.5 for the C_2S/C_3S mixture (obtained by SEM-EDX analyses).

(g) The portlandite and calcite contents of the unaltered HCP were fixed from TG analyses.

(h) Portlandite was considered to be completely depleted in the altered area.

(i) K-shlykovite and straetlingite were used as proxy for ASR-like gel and C-A-S-H + silica gel, respectively. Indeed, these two phases have known chemical compositions and densities and are commonly used as crystalline proxy for these types of amorphous phases (Honorio et al., 2020; Lalan et al., 2016; Zubkova et al., 2010).

(j) The porosity was determined by grey level analyses considering porous products as porosity and slightly adjusted to fit the chemical profiles.

(k) Sorption of dissolved species in hydrated cement phases were not considered. Moreover, partial substitution in either hydrated or unreacted cement phases were not considered.

462 It should be noticed that such simplifications lead to inaccurate microstructural and mineralogical
463 profiles, but sufficiently realistic to be further compared with the modelled mineralogical profiles
464 given in.

465 The chemical profiles were basically calculated based on the amount of phases described above and
466 to their specific gravity. In the calculation procedure, the known/considered volume of
467 phases/components (i.e.: portlandite, C_2S/C_3S,C_4AF, calcite (unaltered area only), porosity) was fixed.
468 Then, the chemical profiles involving one remaining phase were fitted (i.e.; SO_3 was fitted by
469 changing ettringite amount, Fe_2O_3 profile was fitted by changing hydrogarnet amount, MgO was
470 fitted by changing the periclase amount, K_2O was fitted by changing K-schlykovite amount).This
471 procedure allowed to progressively obtain one variable (i.e.; one phase) for one oxide profile.
472 Finally, an individual slight adjustment of the porosity, CaO and SiO_2 profiles was performed. Such
473 adjustment only slightly affect the other chemical profiles.
474 The chemical formula and specific gravity of each phase requested for these assessments are
475 presented in Table 5.

476 The comparison between measured chemical profiles and porosity with expected chemical profiles
477 and porosity from the mineralogical plots are given in Fig. S7 and Fig. S8.
478 The mineralogical profiles are presented in Fig. 8, they highlight the fact that large formation of
479 calcite at the interface, observed by XRD, is necessary to adjust the Ca and Si profiles. Indeed, the
480 precipitation of low Ca/Si phase such as C-S-H 1.2 and ASR-like gel decreases the Ca/Si ratio at the
481 interface and in the area where portlandite is completely dissolved, a Ca rich phase is necessary to
482 compensate replacement of C-S-H 1.6 by C-S-H 1.2. Thus, the formation of quite large amount of
483 ASR-like gel in the SON68 cell (simulated as K-shlykovite) allows to decrease the Ca/Si ratio at the
484 direct interface and explain the difference in the Ca and Si profiles in the two cells.
485 The mineralogical plots also show that ettringite dissolution front is slightly deeper in the SM539 cell,
486 although the portlandite dissolution front is shorter compared to the SON68 cell.
487 The SEM grey level analyses revealed that the overall porosity slightly increases in the altered area,
488 especially for the SON68 cell in which the complete dissolution front of portlandite is deeper.
489 However, this porosity increase due to phase dissolution is partially compensated by precipitation of
490 low Ca/Si C-(A)-S-H in the altered area and of the S.A.P. layer edging the altered HCP. This is
491 particularly visible for the SON68 cell in which this layer is very thick and dense. The dissolution of
492 ettringite is also responsible of the porosity increase in the first 300 µm from the stainless-steel filter.
493 However, the assessment of porosity change where only ettringite is dissolved (not portlandite) was
494 not performed (i.e., grey level analyses were performed in the region 0-200 µm and 0-100 µm to the

stainless-steel filter for SON68 and SM539 cell, respectively and at a distance greater than 500 µm from the interface corresponding to the unaltered area).

3.2 Glass dissolution tracers

In order to follow the migration of boron and lithium released from the glass to the HCP compartment, both elements being considered as good glass dissolution tracers, LA-ICP-MS analyses were carried out in both line and spot ablation mode. The line mode analyses were acquired to obtain mean diffusion profiles for both elements and are presented in the companion paper (Liu et al., 2024, submitted). In addition, the spot analyses were acquired to obtain more informations on the speciation of these elements in the HCP and are presented here.

3.2.1 Boron diffusion

The Fig. 9 shows the measured concentration of boron along with SEM pictures giving the location of the analyses for both cells. In the SM539 cell, the boron concentration is much higher in the S.A.P., either precipitating in the stainless-steel filter (A3) or edging the HCP (A2), than in the porous altered area (A1). This observation suggests that boron is highly retained in the multi-layered gel identified as a mixture of C-A-S-H or Al-containing ASR gel and Si glass. However, this technique cannot probe if boron is either sorbed or incorporated in this layer or if it precipitates as another B-bearing phase. In the SON68 cell, the highest boron concentration value (43000 ppm) is localized in an area enriched in sulphur and aluminium (Fig. 9), suggesting a partial substitution of boron in AFt and/or AFm phases. Such phases were observed at the interface by SEM and µ-Raman only for this cell. The phase identified as an ASR gel in the S.A.P. layer also retains a high amount of boron. However, boron is not specifically retained in the more porous altered area of the HCP where high amount of low Ca/Si C-S-H precipitated. This result suggests that this phase is not a sink for boron and/or that the local conditions (i.e., pH, solution composition) in the altered area were not favourable for the precipitation of B-bearing phases. In the unaltered region of the HCP, fluctuations of the boron concentration were observed in the first 600 µm from the interface (i.e., the decrease in the boron concentration with increasing distance from the interface cannot be described by a simple diffusion process). These fluctuating concentrations are also visible in the boron profiles presented in the companion paper (Liu et al., 2024, submitted). Apart from the ettringite dissolution processes, no major mineralogical changes were observed in this area. This result rather either suggests that the local environment favoured the precipitation of B-bearing phase in this area or that B was quantitavely substituted to S in AFt.

3.2.2 Lithium diffusion

The Fig. 10 shows the measured concentration of lithium along with SEM pictures giving the location of the analyses for both cells. As for boron, the lithium is highly retained in the S.A.P. layers edging the HCP (A2) and precipitating in the filter pores (A3) for both cells. Again, this result suggests that the ASR-like gel is a sink for this glass dissolution tracer. Moreover, the lithium is highly retained in the porous altered area where low Ca/Si C-(A)-S-H are found. This suggests that lithium is either sorbed or incorporated in the structure of this phase, or that it precipitates along with it. Contrary to boron, the concentration of lithium is not fluctuating in the unaltered cement paste as it always decreases, suggesting in all cases a diffusion process. This result implies that the precipitation of lithium in a secondary phase in the unaltered area of the HCP is unlikely.

4 Discussion

4.1 Degradation of the HCP

In both cells, a degradation front is observed in the HCP, and referred as altered area in the previous sections. This degradation front is characterized by a microstructural change (i.e., porous network changes) and dissolution/precipitation processes often encountered in cementitious material in contact with a silicon rich medium (e.g., argillaceous medium (Dauzeres et al., 2010)).

Portlandite depletion was depicted in the first hundreds of micrometers associated with precipitation of C-A-S-H or C-S-H in the porous area. Indeed, the dissolved silica released from the glass compartment can trigger the pozzolanic reaction (i.e., dissolution of portlandite reacting with dissolved silica to form C-S-H). The new C-S-H that formed filled the large pores induced by HCP leaching. This phenomenon was more pronounced in the SON68 cell due to the larger release of silicon from the glass compartment. In the presence of a larger amount of Al (i.e., in the SM539 cell), the phenomenon was also observed and the incorporation of Al in C-S-H occurred. Moreover, the decalcification of former C-S-H might have occurred in the area where portlandite was completely dissolved, as suggested in section 3.1.4. The decalcification process (i.e., portlandite dissolution and degradation of C-S-H), together with ettringite degradation was responsible for the coarse porosity increase observed in the first hundreds of micrometers. Indeed, the coarse porosity in the first 100 µm from the stainless-steel filter was increased by a factor 6 and by 15.5 for the SM539 cell and SON68 cell, respectively. Note that the coarse porosity quantified by SEM grey level analyses only

represents a limited fraction of the HCP porosity. Indeed the porosity of a cement paste can be segmented into air voids, capillary porosity (with pore size ranging from10 nm to 10 µm) and gel porosity (with pore size inferior to 10 nm and down to few tens of nanometers corresponding to the interlayer of the CSH) (Mindess et al., 2003). While such processes induced porosity increase, the neo-formation of Ca-Si gel induced pore clogging, reducing significantly the capillary porosity at the interface. Such precipitation is generating gel porosity that can hinder the diffusion of element towards the HCP. The precipitation of secondary ettringite would also be a mechanism responsible for pore clogging, as observed in HCP degraded in water (Haga et al., 2005). Enrichment in sulphur was not observed at further distance from the degradation front, and S enrichment was observed in the glass alteration layers (not shown), meaning that this element rather migrated from the HCP to the glass compartment. Moreover, carbonation with formation of calcite occurred in the altered area as revealed by XRD for both cells. This latter phenomenon is due to a contamination of atmospheric CO_2 in the glass compartment during the different solution sampling. On the one hand, precipitation of calcite favoured pore clogging and on the other hand, several authors reported that carbonation of hydrated cement phase can increase the porosity (e.g.,(Borges et al., 2012)). Some authors also showed that carbonation is responsible for the increase of the critical pore diameter size in carbonated CEM I paste (e.g., (Borges et al., 2012)). Thus, both carbonation and formation of Ca-Si-(Al) gel are responsible for the increase of gel porosity /capillary porosity ratio. Finally, the release of large amount of dissolved silica, especially in the SON68 cell, enhanced the fast hydration of unreacted clinker (mostly C_3S/C_2S grains) at the interface, resulting in the formation of inner C-S-H. These inner C-S-H are known to exhibit different microstructure compared to outer C-S-H (Richardson, 1999). Indeed, the packing density is higher in inner C-S-H compared to outer C-S-H (Gao et al., 2015). Thus, the cation sorption is more limited in inner C-S-H compared to outer C-S-H. The hydration of these C_2S and C_3S grains was enhanced by the incoming dissolved silica from the glass. Thus, this hydration phenomenon also gives an indirect indication on the diffusion of silicon which could not be measured by the employed techniques. As the increase in the level of hydration was limited to the altered zone, we can reasonably suppose that diffusion of silicon was restricted to this region.

4.2 Alkalis (Li, Na, K) uptake by C-(A)-S-H

The SEM-EDX and LA-ICP-MS analyses revealed a large enrichment in alkalis at the interface between the stainless-steel filter and the HCP for both cells. Li and K are alkali transport tracers from the glass to the cement and from the cement to the glass, respectively, while Na can not be used as a tracer as present in both compartment initially. In Portland cement-based materials, C-S-H is reported to be

596 the major binder of alkali ions, i.e., the amount retained by the other hydrates such as portlandite,
597 ettringite, hydrogarnet and hydrotalcite is negligible (Chappex and Scrivener, 2012). Thus, alkalis are
598 principally sorbed by C-(A)-S-H phases initially present in the hardened OPC paste or formed due to
599 the reaction of Si released by glass dissolution with portlandite. It is well-known that the alkali
600 sorption capacity of C-S-H drastically increase with decreasing Ca/Si ratio (Hong and Glasser, 1999;
601 L'Hôpital et al., 2016; Lothenbach and Nonat, 2015; Miron et al., 2022; Stade, 1989).Moreover, the
602 sorption capacity of C-(A)-S-H phase depends on the incorporated cation itself but the studies draw
603 different conclusions about the preferential incorporation of one alkali against another. For instance,
604 some authors did not observed significant difference between the sorption of Na and K (Hong and
605 Glasser, 1999; L'Hôpital et al., 2016; Stade, 1989) while others expected preferential sorption of K
606 (Bach et al., 2013; Miron et al., 2022). In this latter case, the preferential sorption can be related to
607 structural grounds, because K can substitute Ca in the interlayer whereas Na cannot (Mitchell, L. D.;
608 Margeson, J. C.; Beaudouin, 2007). Stade (1989) observed a large preferential incorporation of Li
609 against both Na and K in C-S-H and this difference was explained by Mitchell et al (2007), who
610 suggested that Li can adopt both tetrahedral and octahedral form in silicates and that Li can
611 substitute Si in the silicate chains. However, this result is in contraction with a recent study that
612 shows no preferential Li incorporation against Na and K (Miron et al., 2022). Finally, Al incorporation
613 in the C-(A)-S-H can have an effect on the sorption capacity and diffusive properties of alkalis.
614 Recently, it was shown by atomistic calculations that the aliovalent substitution of Si by Al in the
615 tetrahedral site induces the creation of new sorption site that enhances sorption of alkalis, and that
616 the diffusivity of alkalis is drastically reduced in C-A-S-H compared to C-S-H due to the stronger
617 electrostatic interaction induced by the substitution (Duque-Redondo et al., 2021). However,
618 experimental data did not show evidence of preferential sorption of alkalis in Al substituted C-S-H
619 (Bach et al., 2013; Brown et al., 2017; Chappex and Scrivener, 2012; L'Hôpital et al., 2016).

620

621 ## 4.3 ASR-like gel formation and role of Al and Li

622 ### 4.3.1 ASR gel formation

623

624 Alkali aggregate reaction is a well-known concrete phenomenon that occurs in the presence of
625 reactive silica aggregates. The reaction of these aggregates with alkalis coming from the cement
626 porewater solution and calcium can lead to the formation of ASR gel that induces cracks in concrete
627 (Dent Glasser and Kataoka, 1981). In our experiments, the source of reactive silica is external to the
628 cement paste. Thus, this phenomenon is limited to the interface between the glass compartment and
629 the HCP.
630 At the dissolution front, the income of Si together with the release of alkalis from both glass network

and HCP, combined with the Ca released from the portlandite dissolution and C-S-H decalcification favoured the precipitation of ASR-like gel. This phenomenon was particularly evident in the SON68 cell where a thick layer of ASR-like gel was observed at the interface (S.A.P. edging the HCP). In the presence of a reactive silica source, calcium and alkalis, it was shown by Hou et al., 2004 that C-S-H are favoured against ASR gel formation in the area where portlandite and/or high Ca/Si C-S-H are available. Thus, it explains why the formation of ASR-like gel, is limited to the dissolution front, despite the large amount of silicon released in the glass compartment (Table S4). However, SEM observations revealed that the newly formed C-S-H further reacted with Si coming from glass leaching to form the ASR-like gel (Fig. S9). Indeed, in the sequence proposed by Hou et al., 2004, the formation of low polymerized C-S-H is followed by the formation of highly polymerized silica after depletion of lime sources. After that, the C-S-H reaches a Q^1/Q^2 ratio = 0.45, which is the highest possible ratio for C-S-H, and gelation of ASR gel starts with further income of Si. Thus, the ASR like gel would propagate toward the HCP with time. The formation of a dense gel at the top of the cement compartment plays a diffusive barrier role and can incorporate or sorb elements from the glass matrix. Indeed, it is well known that alkali silicate water glasses are employed in civil engineering for their sealing properties. It is generally admitted that the addition of alkali silicates at the concrete surface lead to the waterproofing of the concrete surface by formation of calcium silicate gels (Iliushchenko et al., 2022; Jiang et al., 2015; Larosa Thompson et al., 1997; Song et al., 2016). Such phenomenon is observed for both cell even if the nature, thickness and microstructure of the diffusive barrier is different for the two studied glass. Moreover, the large incorporation of element coming from the glass matrix (e.g.; Si,B,Li,Cs,Mo) indicate that this gel can potentially limit the ingress of radionuclides in the nearfield of deep geological repository (DGR). However, further studies would be needed to (i) analyse the radionuclide retention properties of such gel and, (ii) determine the stability field of such phase due to the evolving conditions in Dutch and Belgian DGR system (e.g.; pH decrease in the long term (Kursten and Druyts, 2015; Verhoef et al., 2017)). These informations can be useful with regards to conservative safety assessments.

4.3.2 Role of Al

In the SM539 cell, the amount of Si released from the glass compartment is lower but the Al content is well higher. The phase that precipitated at the interface of the HCP and stainless-steel filter is much thinner than in the SON68 cell and presents a layered structure. In a recent review dealing with the role of Al and Li on ASR mitigation, (Shi and Lothenbach, 2022) proposed that incorporation of Al in ASR gel is unlikely. This assumption is based on an experiment in which they synthetized ASR gel in the presence of an $Al(OH)_3$ source and demonstrated that incorporation of aluminium in ASR gel was not effective and that Al rather precipitated in the form of gibbsite (Shi et al., 2021). In their review

they pointed out that Al is sometimes detected in ASR gel and sometimes not. However, it is true that the Al content detected in the ASR gel formed from diverse reactive aggregates and in various cementitious media does not exceed 2-3 wt. % Al_2O_3 (e.g.; (Fernandes, 2009; Fernandes et al., 2007; Guo et al., 2018; Leemann and Lura, 2013; Shafaatian et al., 2013)). Such low values are well under the 20 wt. % Al_2O_3 observed in this layer. Thus, we suggest that the formation of an ASR-like gel in the SM539 cell was unlikely and C-A-S-H rather precipitated together with a silica gel leading to an edging phase with a layered structure. Indeed, C-S-H can incorporate large amount of Al , especially at high pH, in alkalis rich solutions, with an Al/Si ratio up to 0.23 in 0.5 mol/L KOH solution (L'Hôpital et al., 2015). As the Ca/Si ratio at the interface with the stainless-steel filter was very low and might have even decrease with C-A-S-H precipitation, the precipitation of successive layers of C-A-S-H and silica gel incorporating alkalis might have been promoted.

4.3.3 Role of Li

Lithium is also responsible for mitigating ASR and this element was observed in the ASR-like gel that formed in the SON68 cell. In the review of (Shi and Lothenbach, 2022), an exhaustive description of the parameters influencing the ASR mitigation along with the associated different mechanisms is presented. In particular, the Li salt type, the Li concentration and thus the Li/(Na+K) ratio are influencing parameters on ASR mitigation. The mechanisms involved in ASR mitigation are various and principally rely on either (i) limitation of the silicon dissolution (ii) formation of protective barriers around aggregates and (iii) formation of non-expansive products. In our experiment, the reactive silica and lithium sources have the same origin, which is located at great distance from the HCP, and the amount of lithium released from the glass is very low compared to the minimum concentration required for ASR mitigation (Li/(Na+K) ≈ 0.6). Thus, the mechanisms that are linked to the effect of lithium on silica dissolution or to the formation of protective barriers surrounding aggregates preventing ASR are not of interest for this study. However, lithium can influence the structural properties of the ASR gel. Indeed, lithium can substitute calcium in the interlayer and disrupt the silica chains reducing Q^3 sites in favour of more Q^1 and Q^2 sites (Leemann et al., 2014). Moreover, several authors showed that the incorporation of Li in ASR gel resulted in a dense gel, similar to the one observed in our study (Feng et al., 2010; Leemann et al., 2014). In the present experiment the lithium content in the ASR like-gel is quite low (between 0.1 and 0.3%), but it could have influenced the growth of this gel along with calcium and favoured such type of dense product, which can act as diffusion barrier for dissolved glass elements.

4.4 Zeolite formation

In the stainless-steel filter close to the glass compartment (A4), the important release of aluminium from the glass might have favoured the precipitation of zeolite. Indeed, the S.A.P. in the stainless-steel filter close to the glass compartment have a Ca/Si ratio of 0.1 and an Al/Si ratio of 2.2-2.7, which is rather close to the respective ratios in K-phillipsite. This zeolite phase is thermodynamically predicted in similar systems where Si and Al sources react with alkalis from cementitious materials and is frequently observed in experiments conducted at temperature above 70°C (e.g., cement-clay interface (Blanc et al., 2015; Lalan et al., 2016); cement-aluminous glass interface (Utton et al., 2013); cement-aggregate interface (Lothenbach et al., 2017)). Conversely, this phase is not observed at lower temperature due to kinetic reason (Blanc et al., 2015; Shi et al., 2021).Instead, an amorphous alkali alumina-silicate gel rather precipitates (Lothenbach et al., 2017; Shi and Lothenbach, 2022) and serves as a precursor for zeolite precipitation. This gelation process might have been triggered during our experiments leading to the formation of an amorphous gel that was not detected by XRD. Despite the quite long reaction time of 900 days in fully saturated conditions, nucleation and growth of zeolite crystals was not observed.

4.5 Boron retention

Boron is considered as a good tracer of glass dissolution in a wide range of pH values (acidic to low alkaline) due to its good mobility and because this element is not retained in the glass alteration layer (Suzuki-Muresan et al., 2018). However, this element can interact with the cementitious phases and/or with the porewater solution. Indeed, boron is widely employed as a cement hydration retarder, as it can inhibit $Ca(OH)_2$ nucleation and/or precipitate around unreacted cement grains and limit exchange between porewater solution and clinker phases (Bensted et al., 1991; Csetenyi and Glasser, 1995). In this study, the boron ingress started well after the setting time of the HCP, implying different retention mechanisms. The interaction between boron and cement phases/porewater solution is discussed in this section whereas considerations on boron diffusion behaviour is discussed in the companion paper.

As the porewater chemistry of cement is highly enriched in alkalis and due to the release of Ca at the interface, B-bearing phases belonging to the system Na_2O-K_2O-CaO-B_2O_3-H_2O might have precipitated and can not be observed by the conventional techniques used in this study. Only a few phases belonging to this system are reported to be stable in highly alkaline medium (pH>12) (Apagyi and Csetenyi, 2001; Csetenyi and Glasser, 1995; Dhoury, 2015) . Among these phases, $Na_2B_4O_5(OH)_4$. $8H_2O$ (borax) and $Ca[B(OH)_4](H_2O)_2$ (hexahydroboracite) can form. This latter phase can convert into

733 $Ca[B(OH)4]_2$ (flovolite) in the presence of high amount of Ca and B or at elevated temperature
734 (Dhoury, 2015), and as hexahydroboracite is unstable in the cementitious matrix, it generally
735 transforms into a more stable boro-aluminate phase (Cau Dit Coumes et al., 2017).

736 It is also well-known that AFm and AFt phases can incorporate boron in their crystal lattices (Bothe
737 and Brown, 1998; Champenois et al., 2012; Csetenyi and Glasser, 1993). In the SON68 cell, the
738 largest amount of boron was reported in Al and S rich phase that might correspond to ettringite.
739 Moreover, monocarboaluminate precipitated at the interface in this cell. In this AFm phase, HBO_3^{2-}
740 can substitute CO_3^{2-} groups and form a complete solid solution. In our study, the Raman analyses of
741 this phase did not evidence any structural lattice change or frequency shift in the lattice vibration
742 due to this substitution, but a partial substitution is conceivable.
743 Finally, boron might be retained in the structure of C-S-H or in the structure of the ASR gel.
744 Surprisingly, high amounts of boron were found to be present in the ASR-like gel phases. Indeed,
745 boron diffuses as an anionic species and thus preferentially sorbs on high Ca/Si C-S-H (Labbez et al.,
746 2011). However, it might have been incorporated in the structure of this gel. To the best of our
747 knowledge, there are no studies about incorporation of boron in C-S-H phase and ASR gel. However,
748 (Nozawa et al., 2018) observed co-precipitation of boron with silicon and magnesium in M-S-H, in the
749 presence of magnesium oxide, amorphous silica and $B(OH)_3$ solutions. In their study, they showed
750 that approximately 50% of boron is retained in the precipitates after 18 days of interaction, with an
751 initial concentration of 100 ppm of boron. They suggest that boron can be either isomorphically
752 substituted to the tetrahedral Si or incorporated in triangular planar form in the interlayer of the M-
753 S-H structure.

754

755 5 Conclusion

756 The present work gives a phenomenological description of the HCP evolution in the presence of two
757 types of nuclear borosilicate glass analogues and separated by a stainless-steel filter simulating the
758 canister break. The major findings of this study can be listed as follows:
759 - Degradation of the HCP occurred only close to the glass in the first hundreds of micrometers of the
760 70 mm thick cement paste, leading to decalcification of high Ca/Si C-S-H, dissolution of portlandite
761 and ettringite at the interface and to the precipitation of low Ca/Si C-S-H via the pozzolanic reaction.
762 Depending on the Si amount released from the glass, the degradation is more or less pronounced
763 with a decalcification front of approximately 100 and 200 µm for the SM539 and SON68 glasses,
764 respectively.
765 - The precipitation of a dense amorphous gel is likely to occur both at the interface between glass

compartment and stainless-steel filter and HCP compartment and stainless-steel filter. Such precipitation would lead to pore clogging in the long-term but is rather limited to the direct interface in the experiment. In the vicinity of both glasses, an aluminous rich gel that can be a precursor of zeolite is observed for both studied glass composition. Close to the glass-HCP interface, the Al and Si content released from glass dissolution played a major role on the nature of the precipitates, with probably an ASR-like gel precipitating in the SON68 cell and a mixture of C-A-S-H and silica gel in the SM539 cell. However, the influence of Al concentration is limited to the direct interface as this element is highly retained in these amorphous gels.

- Boron and lithium considered as good glass dissolution tracers are highly retained in the altered area. Specifically, lithium is retained in both the ASR-like gel that formed at the dissolution front and in the first hundreds of micrometers where precipitation of low Ca/Si C-S-H and decalcification of C-S-H occurred. Boron is preferentially retained in the AFm/AFt phase that remain in the S.A.P. layer and is also trapped in the amorphous gel that precipitate at the interface.

These findings, together with more quantitative data, indicate that, in addition to the engineered barrier, the reaction products from glass and cement interaction might constitute another barrier for the migration of species from the glass. However, further research is still needed with regards to, e.g., the stability and sorbing capacity of the reaction products in order to quantitatively evaluate the potential safety functions provided by the reaction products. In addition, such findings can be implemented in coupled reactive transport models that are helpful for the design and safety assesment of the deep geological repository (DGR).

Acknowledgments.

Research funding by the ACED/EURAD H2020 program under grant agreement No 847593 are gratefully acknowledged. We thank Yann Bortoli for his precious help in the dismantling of the cells and Nicolas Stephant for his assist with SEM-EDX analyses.

References

Andriambololona, Z., Godon, N., Vernaz, E., 1991. R717 Glass Alteration in the Presence of Mortar: Effect of the Cement Grade. MRS Proc. 257, 151–158. https://doi.org/10.1557/proc-257-151

Apagyi, Z., Csetenyi, L.J., 2001. Phase equilibrium study in the CaO-K2O-B2O3-H2O system at 25°C. Cem. Concr. Res. 31, 1087–1091. https://doi.org/10.1016/S0008-8846(01)00529-4

Atkinson, A., Everitt, N.M., Guppy, R., 1987. Evolution of pH in a radwaste repository: experimental

simulation of cement leaching. United Kingdom.

Bach, T.T.H., Chabas, E., Pochard, I., Cau Dit Coumes, C., Haas, J., Frizon, F., Nonat, A., 2013. Retention of alkali ions by hydrated low-pH cements: Mechanism and Na +/K+ selectivity. Cem. Concr. Res. 51, 14–21. https://doi.org/10.1016/j.cemconres.2013.04.010

Balachandran, C., Muñoz, J.F., Arnold, T., 2017. Characterization of alkali silica reaction gels using Raman spectroscopy. Cem. Concr. Res. 92, 66–74. https://doi.org/10.1016/j.cemconres.2016.11.018

Bensted, J., Callaghan, I.C., Lepre, A., 1991. Comparative study of the efficiency of various borate compounds as set-retarders of class G oilwell cement. Cem. Concr. Res. 21, 663–668. https://doi.org/10.1016/0008-8846(91)90117-Z

Blanc, P., Vieillard, P., Gailhanou, H., Gaboreau, S., Marty, N., Claret, F., Madé, B., Giffaut, E., 2015. ThermoChimie database developments in the framework of cement/clay interactions. Appl. Geochemistry 55, 95–107. https://doi.org/10.1016/j.apgeochem.2014.12.006

Bonta, M., Eitzenberger, A., Burtscher, S., Limbeck, A., 2016. Quantification of chloride in concrete samples using LA-ICP-MS. Cem. Concr. Res. 86, 78–84. https://doi.org/10.1016/j.cemconres.2016.05.002

Borges, P.H.R., Milestone, N.B., Costa, J.O., Lynsdale, C.J., Panzera, T.H., Christophoro, A.L., 2012. Carbonation durability of blended cement pastes used for waste encapsulation. Mater. Struct. Constr. 45, 663–678. https://doi.org/10.1617/s11527-011-9788-8

Bothe, J. V, Brown, P.W., 1998. Phase equilibria in the system CaO-AI203- B20 3-H20 at 23 ± l°C. Adv. Cem. Res. 10, 121–127.

Brown, A.P., Hillier, S., Brydson, R.M.D., 2017. Quantification of Fe-oxidation state in mixed valence minerals: A geochemical application of EELS revisited. J. Phys. Conf. Ser. 902. https://doi.org/10.1088/1742-6596/902/1/012016

Cau Dit Coumes, C., Dhoury, M., Champenois, J.B., Mercier, C., Damidot, D., 2017. Combined effects of lithium and borate ions on the hydration of calcium sulfoaluminate cement. Cem. Concr. Res. 97, 50–60. https://doi.org/10.1016/j.cemconres.2017.03.006

Champenois, J.B., Mesbah, A., Cau Dit Coumes, C., Renaudin, G., Leroux, F., Mercier, C., Revel, B., Damidot, D., 2012. Crystal structures of Boro-AFm and sBoro-AFt phases. Cem. Concr. Res. 42, 1362–1370. https://doi.org/10.1016/j.cemconres.2012.06.003

828 Chappex, T., Scrivener, K., 2012. Alkali fixation of C-S-H in blended cement pastes and its relation to
829 alkali silica reaction. Cem. Concr. Res. 42, 1049–1054.
830 https://doi.org/10.1016/j.cemconres.2012.03.010

831 Csetenyi, L.J., Glasser, F.P., 1995. Borate retardation of cement set and phase relations in the system
832 Na2O-CaO-B2O3-H2O. Adv. Cem. Res. 7, 13–19. https://doi.org/10.1680/adcr.1995.7.25.13

833 Csetenyi, L.J., Glasser, F.P., 1993. Borate Substituted Ettringites, in: Materials Research Society
834 Symposium. pp. 273–278.

835 Dauzeres, A., Le Bescop, P., Sardini, P., Cau Dit Coumes, C., 2010. Physico-chemical investigation of
836 clayey/cement-based materials interaction in the context of geological waste disposal:
837 Experimental approach and results. Cem. Concr. Res. 40, 1327–1340.
838 https://doi.org/10.1016/j.cemconres.2010.03.015

839 De Craen, M., 2006. The Boom Clay geochemistry: Natural evidence. MRS Online Proc. Libr. 932, 51.
840 https://doi.org/10.1557/PROC-932-5.1

841 Decker, M., Siegel, J., Hilbig, H., Heinz, D., 2021. LA-ICP-MS on hardened cement paste: laser-material
842 interaction, signal formation and optimization of laser fluence. Mater. Struct. Constr. 54, 1–19.
843 https://doi.org/10.1617/s11527-021-01736-4

844 Dent Glasser and Kataoka, 1981. The chemistry of “Alkali-Aggregate” reaction. Cem. Concr. RESEARC
845 11, 1–9.

846 Depierre, S., 2012. Etude des mécanismes d’altération du verre par des eaux cimentaires. Université
847 de Montpellier.

848 Dhoury, M., 2015. Influence des ions lithium et borate sur l’hydratation de ciments sulfo-alumineux :
849 application au conditionnement de résines échangeuses d’ions boratées. Montpellier.

850 Dilnesa, B.Z., Wieland, E., Lothenbach, B., Dähn, R., Scrivener, K.L., 2014. Fe-containing phases in
851 hydrated cements. Cem. Concr. Res. 58, 45–55.
852 https://doi.org/10.1016/j.cemconres.2013.12.012

853 Dodson, V.H., 1990. Pozzolans and the Pozzolanic Reaction, in: Concrete Admixtures. pp. 159–201.
854 https://doi.org/10.1007/978-1-4757-4843-7_7

855 Duque-Redondo, E., Yamada, K., Dolado, J.S., Manzano, H., 2021. Microscopic mechanism of
856 radionuclide Cs retention in Al containing C-S-H nanopores. Comput. Mater. Sci. 190, 110312.
857 https://doi.org/10.1016/j.commatsci.2021.110312

Elia, A., Ferrand, K., Lemmens, K., 2016. Determination of the Forward Dissolution Rate for International Simple Glass in Alkaline Solutions Alice Elia, Karine Ferrand and Karel Lemmens SCK•CEN, Belgian Nuclear Research Centre , Boeretang 200 - BE-2400 Mol, Belgium. MRS Adv. 661–667. https://doi.org/10.1557/adv.2016.

Feng, X., Thomas, M.D.A., Bremner, T.W., Folliard, K.J., Fournier, B., 2010. New observations on the mechanism of lithium nitrate against alkali silica reaction (ASR). Cem. Concr. Res. 40, 94–101. https://doi.org/10.1016/j.cemconres.2009.07.017

Fernandes, I., 2009. Composition of alkali-silica reaction products at different locations within concrete structures. Mater. Charact. 60, 655–668. https://doi.org/10.1016/j.matchar.2009.01.011

Fernandes, I., Noronha, F., Teles, M., 2007. Examination of the concrete from an old Portuguese dam: Texture and composition of alkali-silica gel. Mater. Charact. 58, 1160–1170. https://doi.org/10.1016/j.matchar.2007.04.007

Ferrand, K., Caes, S., Lemmens, K., Liu, S., Meert, K., 2022. Static dissolution experiments under hyperalkaline conditions with dispersed and confined SM539 glass. MRS Adv. 7, 95–99. https://doi.org/10.1557/s43580-022-00214-5

Ferrand, K., Klinkenberg, M., Caes, S., Poonoosamy, J., Van Renterghem, W., Barthel, J., Lemmens, K., Bosbach, D., Brandt, F., 2021. Dissolution kinetics of international simple glass and formation of secondary phases at very high surface area to solution ratio in young cement water. Materials (Basel). 14, 1–22. https://doi.org/10.3390/ma14051254

Ferrand, K., Liu, S., Lemmens, K., 2018. Integrated leach tests with simulated HLW glass in contact with ordinary Portland cement paste, Topical Report.

Ferrand, K., Liu, S., Lemmens, K., 2013. The interaction between nuclear waste glass and ordinary portland cement. Int. J. Appl. Glas. Sci. 4, 328–340. https://doi.org/10.1111/ijag.12047

Gagnon, J.E., Fryer, B.J., Samson, I.M., Williams-Jones, A.E., 2008. Quantitative analysis of silicate certified reference materials by LA-ICPMS with and without an internal standard. J. Anal. At. Spectrom. 23, 1529–1537. https://doi.org/10.1039/b801807n

Gao, P., Ye, G., Wei, J., Yu, Q., 2015. Multi-scale simulation of capillary pores and gel pores in Portland cement paste. 14th Int. Congr. Chem. Cem. Proc. 31, 1–14.

Gastel, M., Becker, J.S., Küppers, G., Dietze, H.J., 1997. Determination of long-lived radionuclides in concrete matrix by laser ablation inductively coupled plasma mass spectrometry. Spectrochim.

889 Acta - Part B At. Spectrosc. 52, 2051–2059. https://doi.org/10.1016/S0584-8547(97)00111-0

890 Gens, R., Bel, J., Pourbaix, A., Hélie, M., Wickham, S., Bennett, D., 2006. Corrosion processes and the
891 expected evolution, of the BSC-1 Supercontainer design for disposal of Belgian HLW and spent
892 fuel. J. Phys. IV JP 136, 13–23. https://doi.org/10.1051/jp4:2006136003

893 Gharibi, E., Jabri, M., Ramdani, A., 2017. The effect of magnesium on the alite phase structural
894 stability and its hydration process. J. Mater. Environ. Sci. 8, 1312–1319.

895 Gin, S., Mestre, J.P., 2001. SON 68 nuclear glass alteration kinetics between pH 7 and pH 11.5. J. Nucl.
896 Mater. 295, 83–96. https://doi.org/10.1016/S0022-3115(01)00434-2

897 Guo, S., Dai, Q., Sun, X., Xiao, X., Si, R., Wang, J., 2018. Reduced alkali-silica reaction damage in
898 recycled glass mortar samples with supplementary cementitious materials. J. Clean. Prod. 172,
899 3621–3633. https://doi.org/10.1016/j.jclepro.2017.11.119

900 Haga, K., Shibata, M., Hironaga, M., Tanaka, S., Nagasaki, S., 2005. Change in pore structure and
901 composition of hardened cement paste during the process of dissolution. Cem. Concr. Res. 35,
902 943–950. https://doi.org/10.1016/j.cemconres.2004.06.001

903 Hong, S.Y., Glasser, F.P., 1999. Alkali binding in cement pastes : Part I. The C-S-H phase. Cem. Concr.
904 Res. 29, 1893–1903. https://doi.org/10.1016/S0008-8846(99)00187-8

905 Honorio, T., Chemgne Tamouya, O.M., Shi, Z., Bourdot, A., 2020. Intermolecular interactions of
906 nanocrystalline alkali-silica reaction products under sorption. Cem. Concr. Res. 136, 106155.
907 https://doi.org/10.1016/j.cemconres.2020.106155

908 Hu, C., Ma, H., 2016. Statistical analysis of backscattered electron image of hydrated cement paste.
909 Adv. Cem. Res. 28, 469–474. https://doi.org/10.1680/jadcr.16.00002

910 Iliushchenko, V., Kalina, L., Hruby, P., Bilek, J., Fladr, J., Bily, P., Bojanovsky, J., 2022. The treatment of
911 cementitious surface by selected silicate sealers. J. Phys. Conf. Ser. 2341.
912 https://doi.org/10.1088/1742-6596/2341/1/012003

913 Jiang, L., Xue, X., Zhang, W., Yang, J., Zhang, H., Li, Y., Zhang, R., Zhang, Z., Xu, L., Qu, J., Song, J., Qin,
914 J., 2015. The investigation of factors affecting the water impermeability of inorganic sodium
915 silicate-based concrete sealers. Constr. Build. Mater. 93, 729–736.
916 https://doi.org/10.1016/j.conbuildmat.2015.06.001

917 Kirkpatrick, R.J., Yarger, J.L., McMillan, P.F., Yu, P., Cong, X., 1997. Raman spectroscopy of C-S-H,
918 tobermorite, and jennite. Adv. Cem. Based Mater. 5, 93–99. https://doi.org/10.1016/S1065-

919 7355(97)00001-1

920 Kursten, B., Druyts, F., 2015. Assessment of the uniform corrosion behaviour of carbon steel
921 radioactive waste packages with respect to the disposal concept in the geological Dutch Boom
922 Clay formation OPERA-PU-SCK513.

923 L'Hôpital, E., Lothenbach, B., Le Saout, G., Kulik, D., Scrivener, K., 2015. Incorporation of aluminium in
924 calcium-silicate-hydrates. Cem. Concr. Res. https://doi.org/10.1016/j.cemconres.2015.04.007

925 L'Hôpital, E., Lothenbach, B., Scrivener, K., Kulik, D.A., 2016. Alkali uptake in calcium alumina silicate
926 hydrate (C-A-S-H). Cem. Concr. Res. 85, 122–136.
927 https://doi.org/10.1016/j.cemconres.2016.03.009

928 Labbez, C., Pochard, I., Jönsson, B., Nonat, A., 2011. C-S-H/solution interface: Experimental and
929 Monte Carlo studies. Cem. Concr. Res. 41, 161–168.
930 https://doi.org/10.1016/j.cemconres.2010.10.002

931 Lafuente B, Downs R T, Yang H, S.N., 2015. The power of databases: the RRUFF project., in: Highlights
932 Mineralogical Crystallography, T Armbruster and R M Danisi, Eds. Berlin, Germany, W. De
933 Gruyter. pp. 1–30.

934 Lalan, P., 2016. Influence d ' une température de 70 ° C sur la géochimie , la microstructure et la
935 diffusion aux interfaces béton / argile : expérimentations en laboratoire , in situ et modélisation
936 To cite this version : HAL Id : tel-01710583 de l ' Université de recher.

937 Lalan, P., Dauzères, A., De Windt, L., Bartier, D., Sammaljärvi, J., Barnichon, J.D., Techer, I., Detilleux,
938 V., 2016. Impact of a 70 °c temperature on an ordinary Portland cement paste/claystone
939 interface: An in situ experiment. Cem. Concr. Res. 83, 164–178.
940 https://doi.org/10.1016/j.cemconres.2016.02.001

941 Larosa Thompson, J., Silsbee, M.R., Gill, P.M., Scheetz, B.E., 1997. Characterization of silicate sealers
942 on concrete. Cem. Concr. Res. 27, 1561–1567.

943 Leemann, A., Lörtscher, L., Bernard, L., Le Saout, G., Lothenbach, B., Espinosa-Marzal, R.M., 2014.
944 Mitigation of ASR by the use of LiNO3 - Characterization of the reaction products. Cem. Concr.
945 Res. 59, 73–86. https://doi.org/10.1016/j.cemconres.2014.02.003

946 Leemann, A., Lura, P., 2013. E-modulus of the alkali-silica-reaction product determined by micro-
947 indentation. Constr. Build. Mater. 44, 221–227.
948 https://doi.org/10.1016/j.conbuildmat.2013.03.018

Leemann, A., Shi, Z., Lindgård, J., 2020. Characterization of amorphous and crystalline ASR products formed in concrete aggregates. Cem. Concr. Res. 137, 106190. https://doi.org/10.1016/j.cemconres.2020.106190

Liu, S., Ferrand, K., Goethals, J., David, K., Lemmens, K., 2024. Model validation and interpretation of the interaction between glass and cement in an integrated glass dissolution experiment. Submitt. to Appl. Geochemistry.

Liu, S., Ferrand, K., Lemmens, K., 2015. Transport- and surface reaction-controlled SON68 glass dissolution at 30°C and 70°C and pH=13.7. Appl. Geochemistry 61, 302–311. https://doi.org/10.1016/j.apgeochem.2015.06.014

Lothenbach, B., Bernard, E., Mäder, U., 2017. Zeolite formation in the presence of cement hydrates and albite. Phys. Chem. Earth 99, 77–94. https://doi.org/10.1016/j.pce.2017.02.006

Lothenbach, B., Nonat, A., 2015. Calcium silicate hydrates: Solid and liquid phase composition. Cem. Concr. Res. 78, 57–70. https://doi.org/10.1016/j.cemconres.2015.03.019

Lothenbach, B, Durdzinski.P, DeWeerdt.K, 2016. Chapter Thermogravimetric analysis, in: Scrivener, K., Snellings, R., Lothenbach, Barbara (Eds.), A Practical Guide to Microstructural Analysis of Cementitious Materials. Taylor and Francis group, Boca Raton, pp. 1–531. https://doi.org/10.1201/b19074

Machner, A., Zajac, M., Ben Haha, M., Kjellsen, K.O., Geiker, M.R., De Weerdt, K., 2018. Limitations of the hydrotalcite formation in Portland composite cement pastes containing dolomite and metakaolin. Cem. Concr. Res. 105, 1–17. https://doi.org/10.1016/j.cemconres.2017.11.007

Mann, C., Ferrand, K., Liu, S., Eskelsen, J.R., Pierce, E., Lemmens, K., Corkhill, C., 2019. Influence of young cement water on the corrosion of the International Simple Glass. npj Mater. Degrad. 3. https://doi.org/10.1038/s41529-018-0059-9

Mindess, S., Young, J.F., Darwin, D., 2003. Concrete, Prentice-Hall civil engineering and engineering mechanics series. Prentice Hall.

Miron, G.D., Kulik, D.A., Yan, Y., Tits, J., Lothenbach, B., 2022. Extensions of CASH+ thermodynamic solid solution model for the uptake of alkali metals and alkaline earth metals in C-S-H. Cem. Concr. Res. 152, 106667. https://doi.org/10.1016/j.cemconres.2021.106667

Mitchell, L. D.; Margeson, J. C.; Beaudouin, J.J., 2007. Synthesis and characterization of lithium and sodium doped C-S-H, in: 12th International Congress on the Chemistry of Cement,July 8-13. Montreal, pp. 1–17.

Nozawa, S., Sato, T., Otake, T., 2018. Effect of dissolved silica on immobilization of boron by magnesium oxide. Minerals 8. https://doi.org/10.3390/min8020076

Ortaboy, S., Li, J., Geng, G., Myers, R.J., Monteiro, P.J.M., Maboudian, R., Carraro, C., 2017. Effects of CO2 and temperature on the structure and chemistry of C-(A-)S-H investigated by Raman spectroscopy. RSC Adv. 7, 48925–48933. https://doi.org/10.1039/c7ra07266j

Rajabipour, F., Giannini, E., Dunant, C., Ideker, J.H., Thomas, M.D.A., 2015. Alkali-silica reaction: Current understanding of the reaction mechanisms and the knowledge gaps. Cem. Concr. Res. 76, 130–146. https://doi.org/10.1016/j.cemconres.2015.05.024

Ribet, S., Gin, S., 2004. Role of neoformed phases on the mechanisms controlling the resumption of SON68 glass alteration in alkaline media. J. Nucl. Mater. 324, 152–164. https://doi.org/10.1016/j.jnucmat.2003.09.010

Richardson, I.G., 1999. Nature of C-S-H in hardened cements. Cem. Concr. Res. 29, 1131–1147. https://doi.org/10.1016/S0008-8846(99)00168-4

Roduit, N., 2007. JMicroVision: Image analysis toolbox for measuring and quantifying components of high-definition images. Version 1.2.7.

Scrivener, K.L., 2004. Backscattered electron imaging of cementitious microstructures: Understanding and quantification. Cem. Concr. Compos. 26, 935–945. https://doi.org/10.1016/j.cemconcomp.2004.02.029

Shafaatian, S.M.H., Akhavan, A., Maraghechi, H., Rajabipour, F., 2013. How does fly ash mitigate alkali-silica reaction (ASR) in accelerated mortar bar test (ASTM C1567)? Cem. Concr. Compos. 37, 143–153. https://doi.org/10.1016/j.cemconcomp.2012.11.004

Shi, Z., Lothenbach, B., 2022. Role of Aluminum and Lithium in Mitigating Alkali-Silica Reaction—A Review. Front. Mater. 8, 1–16. https://doi.org/10.3389/fmats.2021.796396

Shi, Z., Ma, B., Lothenbach, B., 2021. Effect of Al on the formation and structure of alkali-silica reaction products. Cem. Concr. Res. 140, 106311. https://doi.org/10.1016/j.cemconres.2020.106311

Song, Z., Xue, X., Li, Y., Yang, J., He, Z., Shen, S., Jiang, L., Zhang, W., Xu, L., Zhang, H., Qu, J., Ji, W., Zhang, T., Huo, L., Wang, B., Lin, X., Zhang, N., 2016. Experimental exploration of the waterproofing mechanism of inorganic sodium silicate-based concrete sealers. Constr. Build. Mater. 104, 276–283. https://doi.org/10.1016/j.conbuildmat.2015.12.069

Stade, H., 1989. On the reaction of C-S-H (di, poly) with alkali hydroxides 19, 802–810.

Suzuki-Muresan, T., Abdelouas, A., Landesman, C., Ait-Chaou, A., El Mendili, Y., Ribet, S., Perrigaud, K., Shitara, D., Martin, C., Bourbon, X., 2018. Alteration of vitrified intermediate level nuclear waste in alkaline media: effects of cementitious materials, pH and temperature. RSC Adv. 8, 37665–37680. https://doi.org/10.1039/c8ra05227a

Torréns-Martín, D., Fernández-Carrasco, L., Martínez-Ramírez, S., Ibáñez, J., Artús, L., Matschei, T., 2013. Raman spectroscopy of anhydrous and hydrated calcium aluminates and sulfoaluminates. J. Am. Ceram. Soc. 96, 3589–3595. https://doi.org/10.1111/jace.12535

Utton, C.A., Hand, R.J., Bingham, P.A., Hyatt, N.C., Swanton, S.W., Williams, S.J., 2013. Dissolution of vitrified wastes in a high-pH calcium-rich solution. J. Nucl. Mater. 435, 112–122. https://doi.org/10.1016/j.jnucmat.2012.12.032

van Elteren, J.T., Tennent, N.H., Šelih, V.S., 2009. Multi-element quantification of ancient/historic glasses by laser ablation inductively coupled plasma mass spectrometry using sum normalization calibration. Anal. Chim. Acta 644, 1–9. https://doi.org/10.1016/j.aca.2009.04.025

Verhoef, E., Neeft, E., Chapman, N., McCombie, C., 2017. COVRA: OPERA Safety Case. COVRA Publ. 1–147.

Wang, L., 2009. Near-field chemistry of a HLW / SF repository in Boom Clay - scoping calculations relevant to the supercontainer design.

Wickham, S.M., Crawford, M.B., Bennett, D.G., 2005. Belgian Supercontainer Design for HLW and Spent Fuel Disposal. Eval. Ref. Des. Galson Sci. LTD, Oakham.

Zubkova, N. V, Filinchuk, Y.E., Pekov, I. V, Pushcharovsky, D., Yu. Gobechiya, E.R., 2010. Crystal structures of shlykovite and cryptophyllite: comparative crystal chemistry of phyllosilicate minerals of the mountainite family. Eur. J. Mineral. 22, 547–555. https://doi.org/10.1127/0935-1221/2010/0022-2041

Data availability

The raw/processed data required to reproduce these findings can be shared upon request.

Figure captions

Figure 1: Experimental set-up for the integrated tests (hardened ordinary Portland cement paste/stainless-steel filter/glass powder).

Figure 2: EDX mapping (a) and SEM micrograph (b) of the interface between stainless-steel filter and HCP in the SON68 cell after 2430 days of interaction. Identified phases are brownmillerite (C_4AF), alite (C_3S), belite (C_2S), Inner hydration products (Inner HP) and Secondary alteration products (S.A.P.). Zoom on the low Ca/Si C-S-H phase showing its fibrous morphology (c). The unaltered area, altered area and the area with S.A.P. edging the HCP compartment are denoted as area A0, A1 and A2, respectively.

Figure 3: EDX mapping (a) and SEM micrograph (b) of the interface between SS filter and HCP in the SM539 cell after 2430 days of interaction. Identified phases are brownmillerite (C_4AF), alite (C_3S), belite (C_2S), Inner hydration products (Inner HP), Prtl (portlandite), monosulfoaluminate and ettringite mixture (S-containing AFt/AFm mixture), and Secondary alteration products (S.A.P.). The unaltered area, altered area and the area with S.A.P. edging the HCP compartment are denoted as area A0, A1 and A2, respectively.

Figure 4: XRD pattern of the HCP slice collected in the unaltered area and at the interface with the stainless-steel filter for the SM539 (a) and SON68 (b) cells

Figure 5: (K+Na)/(Si+Al) (a) and Al/Si (b) atomic ratios of the newly formed precipitates in function of their Ca/(Si+Al) ratio at different locations in the cells together with the locations of the area where the analyses were performed (c).

.

Figure 6: Raman spectra of the precipitates localized at the interface between the stainless-steel filter and the HCP in the SON68 cell and in the SM539 cell along with the BSE-SEM picture localizing the analysed areas (d). The scale bare correspond to 100µm.

Figure 7: LA-ICP-MS profile measurements of major constituting elements across the hydrated cement paste for the SON68 (a) cell for the SM539 cell (b). The measurements are obtained from NIST 1881b standard. The standard deviations are given at 95% confidence interval. Dots are connected for a better visualization. The concentration of pristine glasses and cement clinker are given as dotted lines at left and right side of the graphs, respectively. SEM images of the profile area after laser ablation are shown for SON68 (c) and SM539 (d) cells.

Figure 8: Mineralogical profiles determined from the solid characterisation analyses and the chemical profiles.

Figure 9: Boron measurement collected by LA-ICP-MS in spot ablation mode along with the location of the analyses in BSE SEM images for (a) SON 68 containing cell and (b) SM 539 containing cell.

Figure 10: Boron measurement collected by LA-ICP-MS in spot ablation mode along with the location of the analyses in BSE SEM images for (a) SON 68 containing cell and (b) SM 539 containing cell.

Table captions

Table 1: Nominal composition of the glasses in mass %.

Table 2: Average analytical composition in weight % of CEM I 42.5 HSR LA Portland cement provided by CIBELCOR®

Table 3: Element concentrations (mol/L) and pH of the YCWCa.

Table 4: Formulas and specific gravity of the phases chosen for the determination of mineralogical profiles in the HCP.

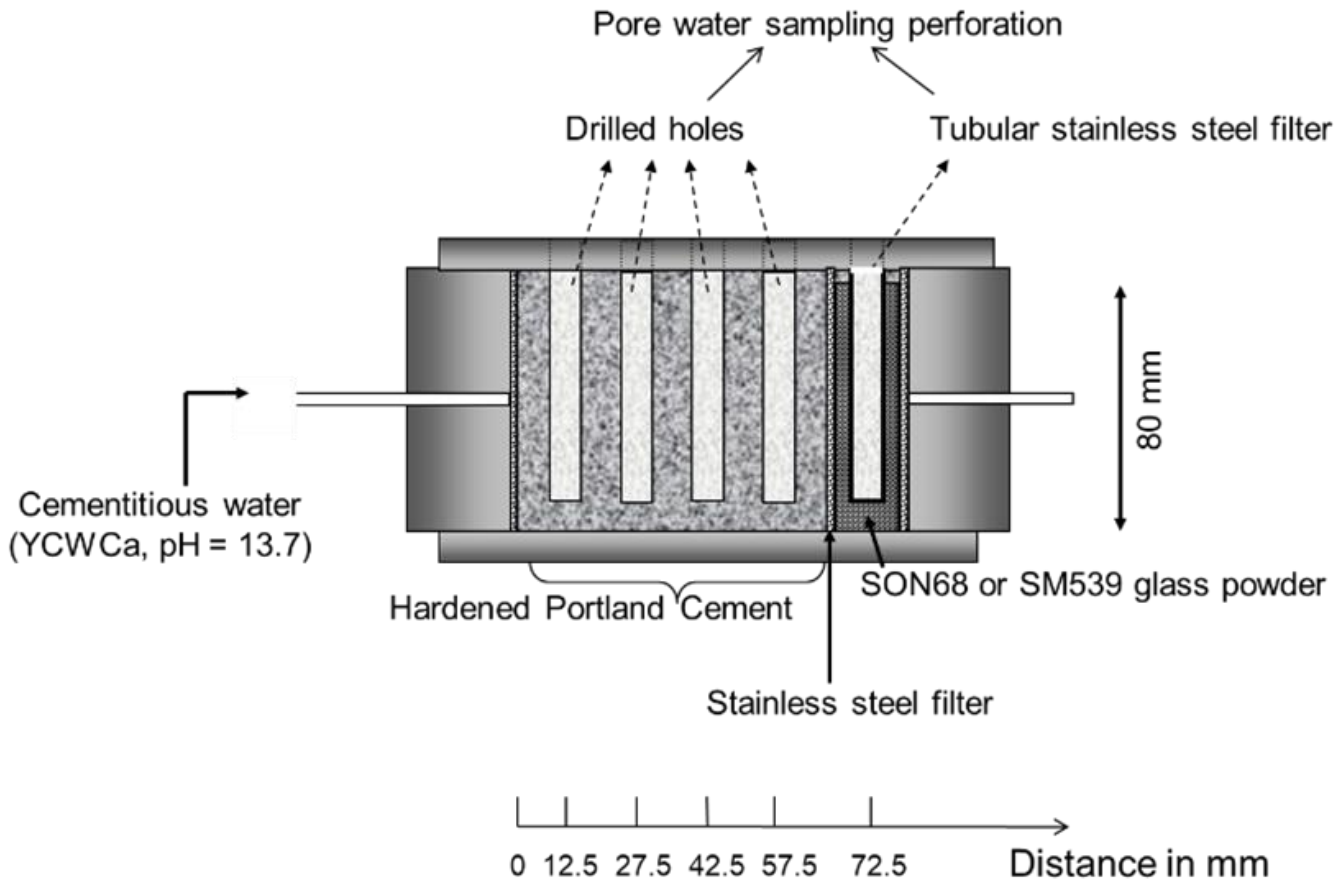
Pore water sampling perforation
Drilled holes
Tubular stainless steel filter
80 mm
Cementitious water
(YCWCa, pH = 13.7)
Hardened Portland Cement
SON68 or SM539 glass powder
Stainless steel filter
0 12.5 27.5 42.5 57.5 72.5
Distance in mm

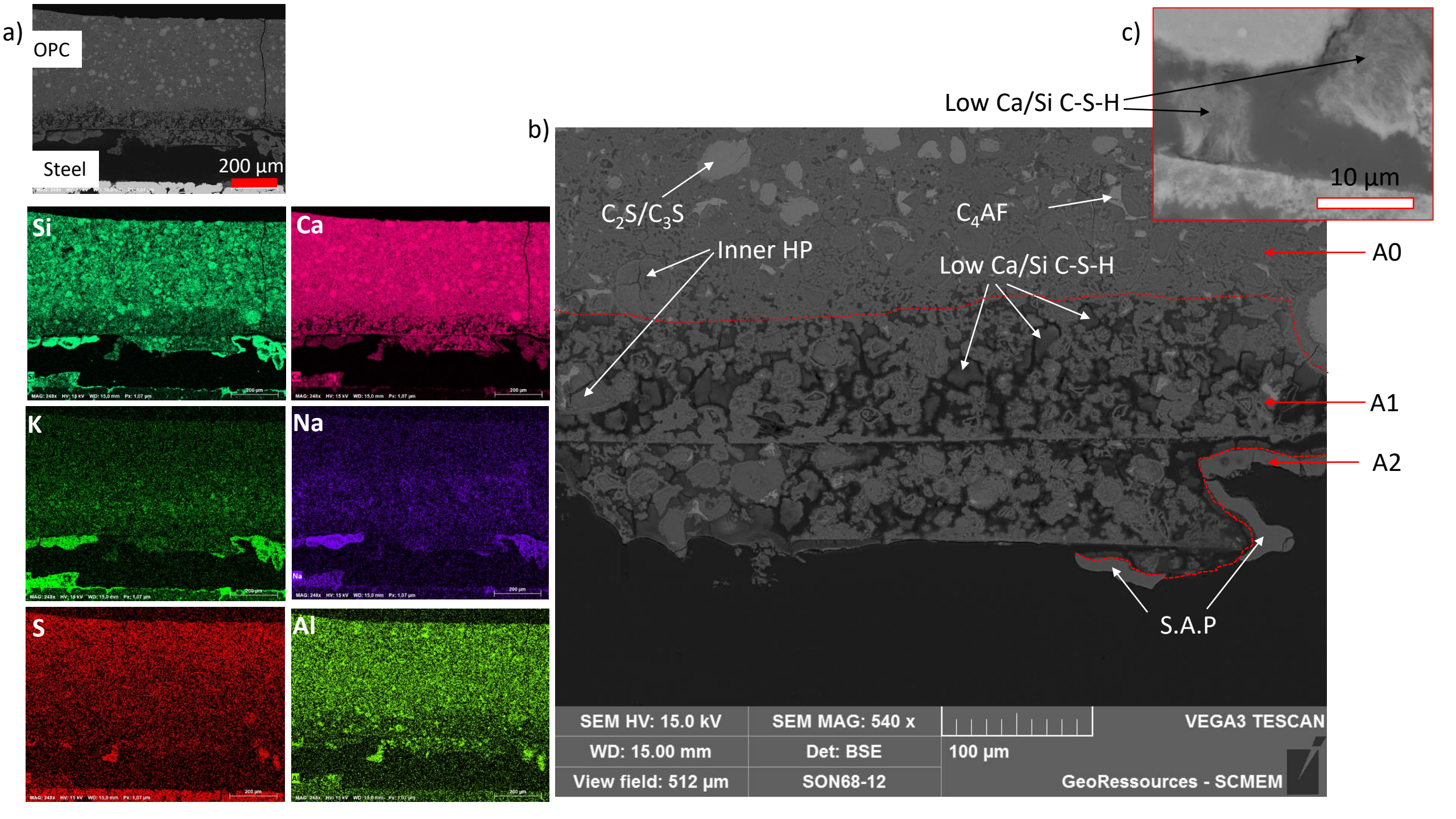
a)
OPC
Steel
200 µm
Si
Ca
K
Na
S
Al
b)
C_2S/C_3S
Inner HP
C_4AF
Low Ca/Si C-S-H
A0
A1
A2
S.A.P
SEM HV: 15.0 kV
SEM MAG: 540 x
VEGA3 TESCAN
WD: 15.00 mm
Det: BSE
100 µm
View field: 512 µm
SON68-12
GeoRessources - SCMEM
c)
Low Ca/Si C-S-H
10 µm

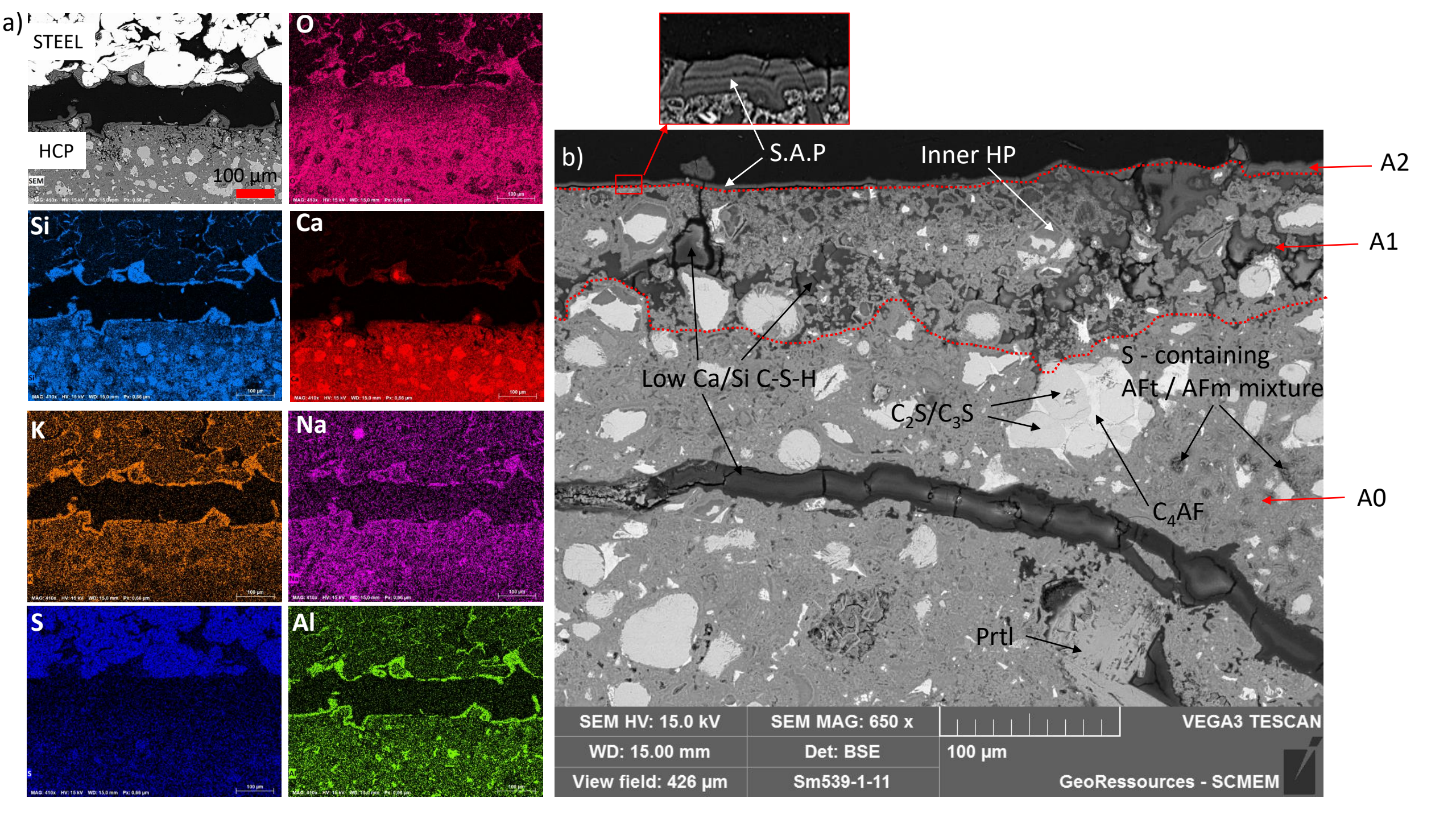
a)
STEEL
HCP
100 µm
O
Si
Ca
K
Na
S
Al
b)
S.A.P
Inner HP
A2
A1
A0
Low Ca/Si C-S-H
C_2S/C_3S
S - containing
AFt / AFm mixture
C_4AF
Prtl
SEM HV: 15.0 kV
SEM MAG: 650 x
VEGA3 TESCAN
WD: 15.00 mm
Det: BSE
100 µm
View field: 426 µm
Sm539-1-11
GeoRessources - SCMEM

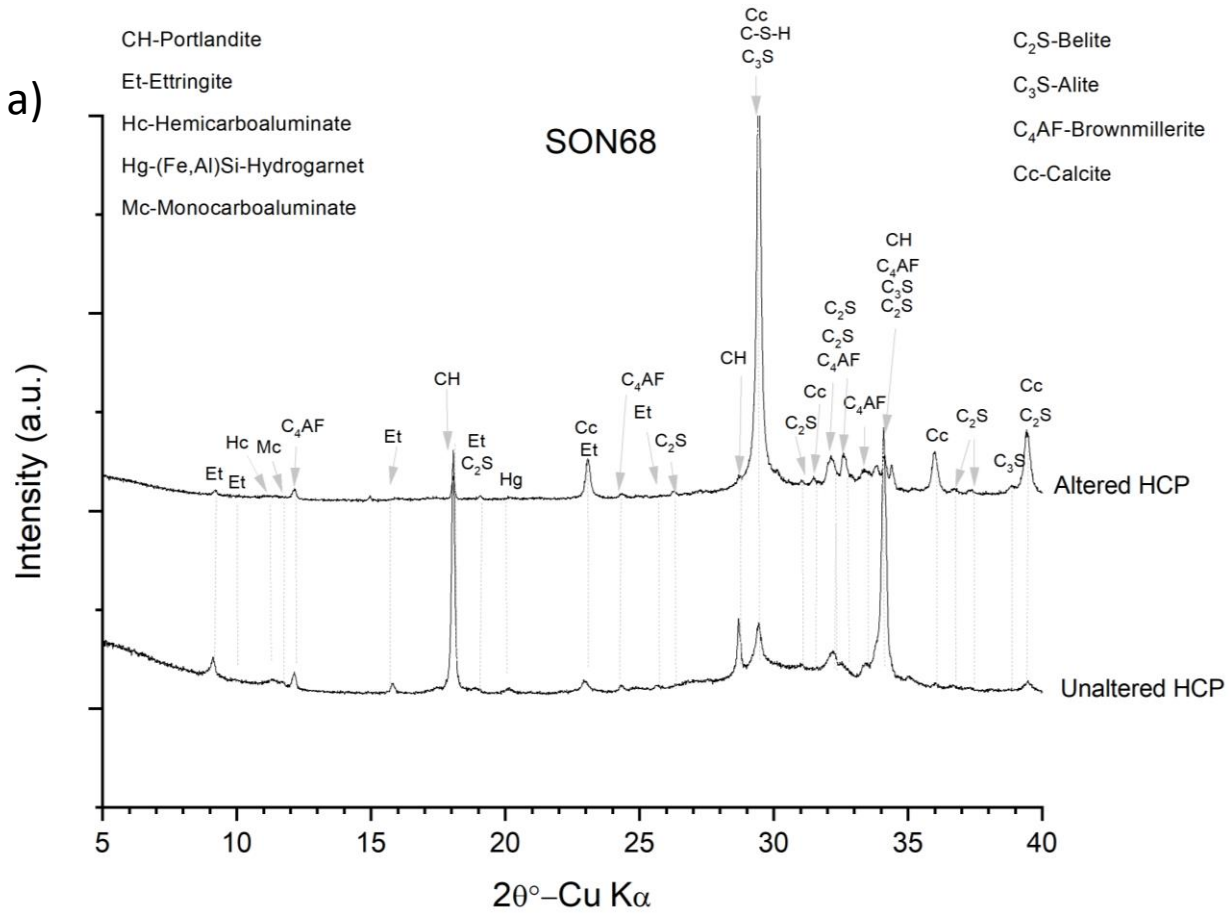
a)
CH-Portlandite
Et-Ettringite
Hc-Hemicarboaluminate
Hg-(Fe,Al)Si-Hydrogarnet
Mc-Monocarboaluminate
SON68
C2S-Belite
C3S-Alite
C4AF-Brownmillerite
Cc-Calcite
Intensity (a.u.)
2θ°–Cu Kα
Altered HCP
Unaltered HCP

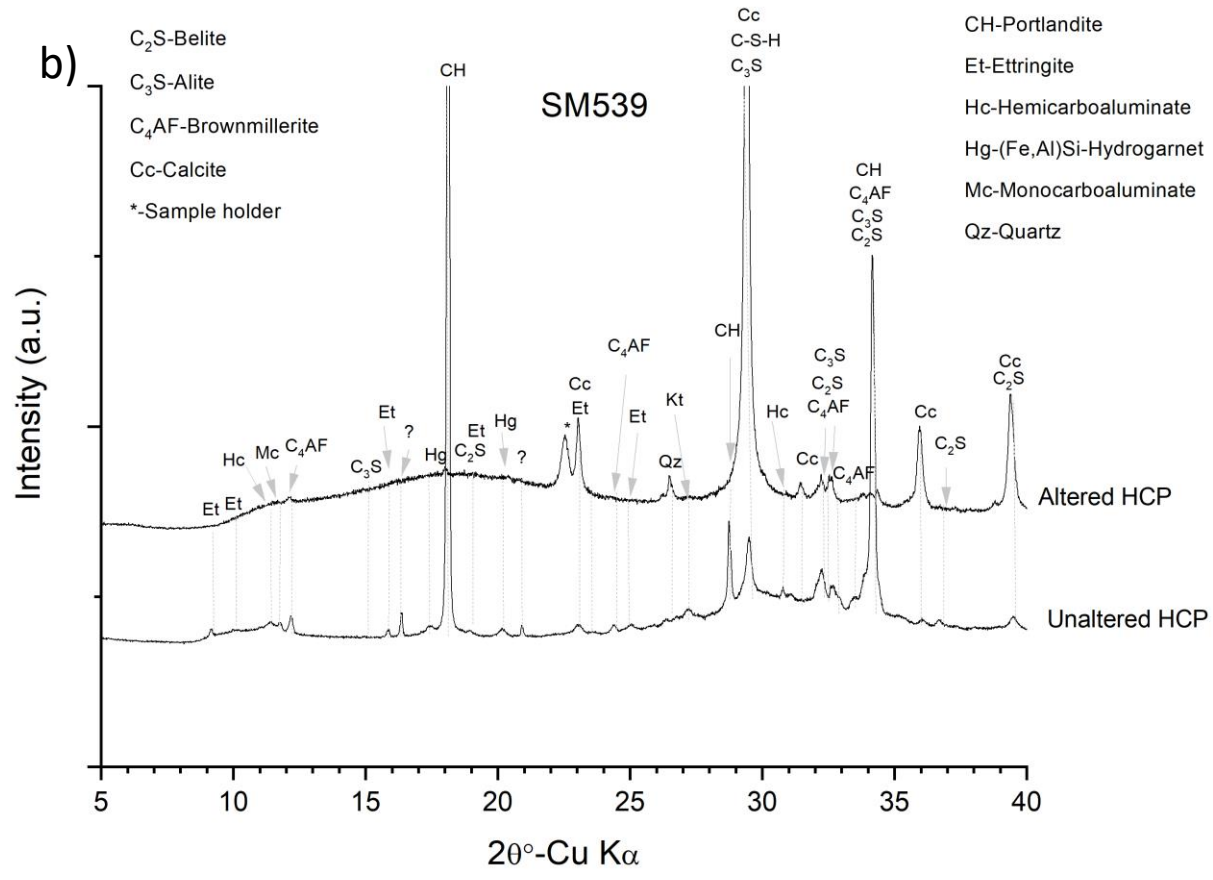
b)
C2S-Belite
C3S-Alite
C4AF-Brownmillerite
Cc-Calcite
*-Sample holder
SM539
CH-Portlandite
Et-Ettringite
Hc-Hemicarboaluminate
Hg-(Fe,Al)Si-Hydrogarnet
Mc-Monocarboaluminate
Qz-Quartz
Intensity (a.u.)
2θ°-Cu Kα
Altered HCP
Unaltered HCP

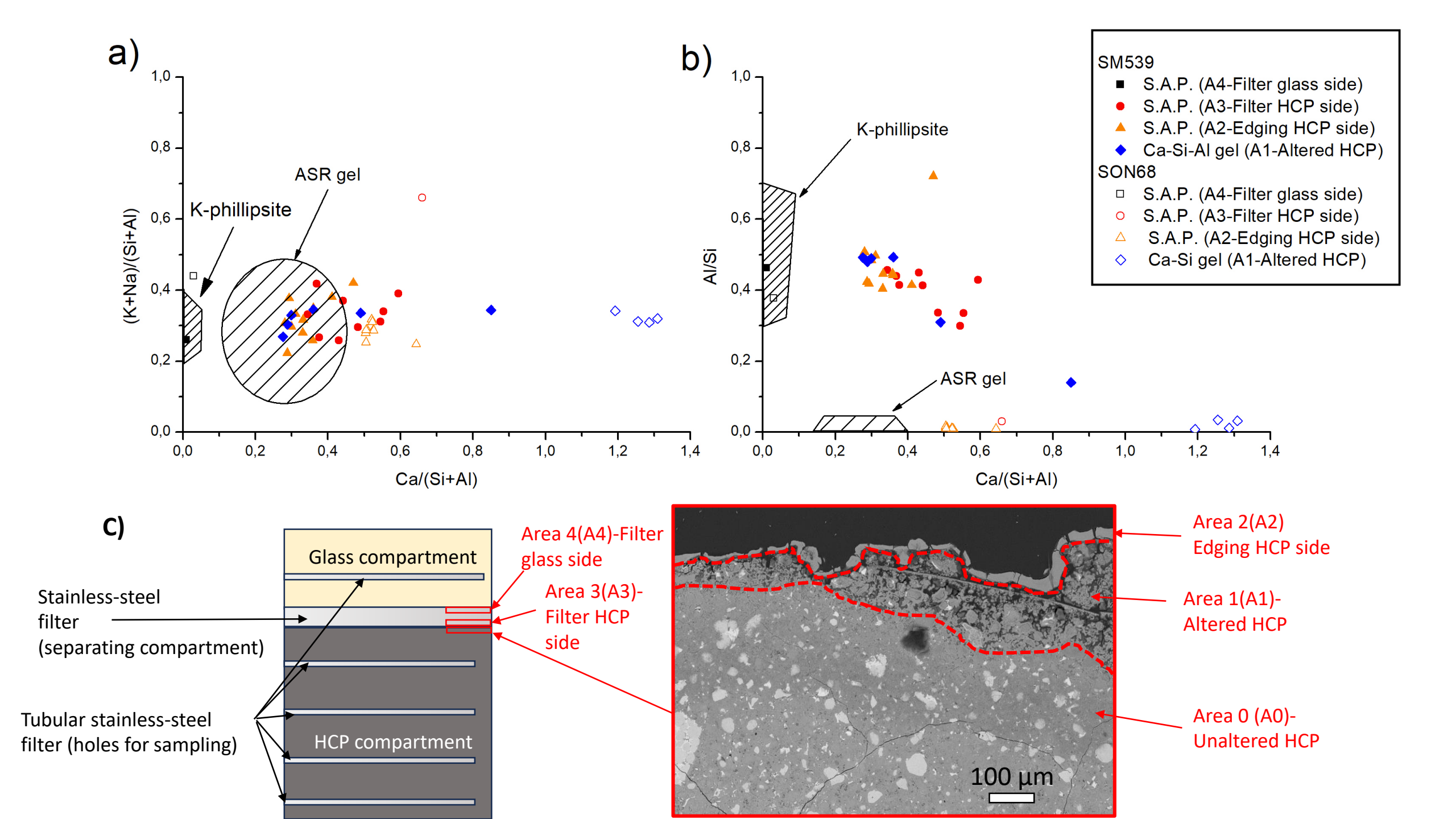
a)
(K+Na)/(Si+Al)
Ca/(Si+Al)
K-phillipsite
ASR gel
b)
Al/Si
Ca/(Si+Al)
K-phillipsite
ASR gel
SM539
S.A.P. (A4-Filter glass side)
S.A.P. (A3-Filter HCP side)
S.A.P. (A2-Edging HCP side)
Ca-Si-Al gel (A1-Altered HCP)
SON68
S.A.P. (A4-Filter glass side)
S.A.P. (A3-Filter HCP side)
S.A.P. (A2-Edging HCP side)
Ca-Si gel (A1-Altered HCP)
c)
Glass compartment
HCP compartment
Stainless-steel filter (separating compartment)
Tubular stainless-steel filter (holes for sampling)
Area 4(A4)-Filter glass side
Area 3(A3)-Filter HCP side
Area 2(A2) Edging HCP side
Area 1(A1)-Altered HCP
Area 0 (A0)-Unaltered HCP
100 µm

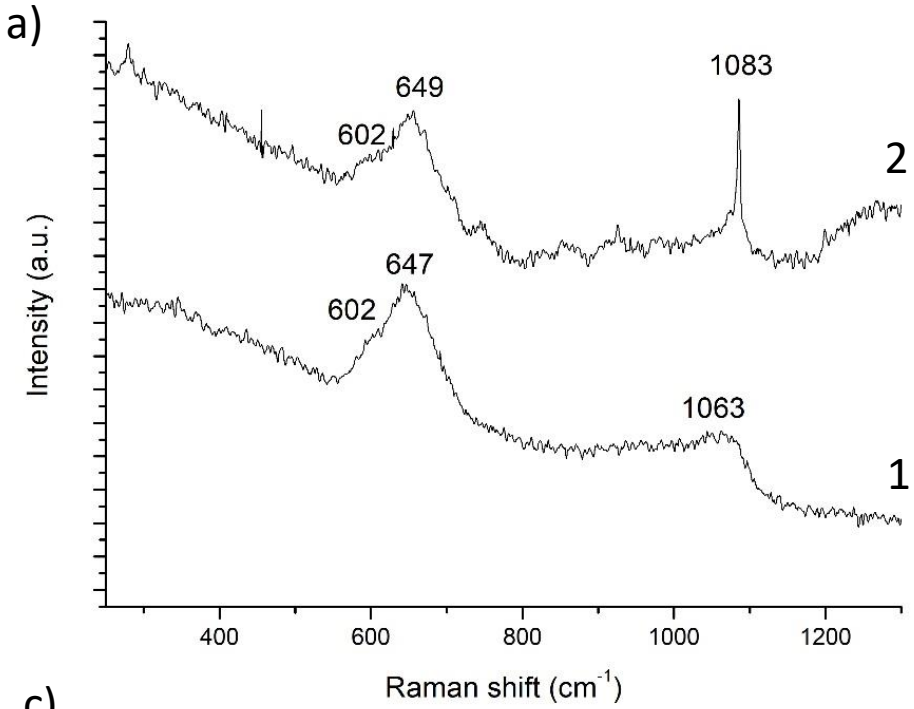
a)
Intensity (a.u.)
649
602
1083
2
647
602
1063
1
400
600
800
1000
1200
Raman shift (cm-1)

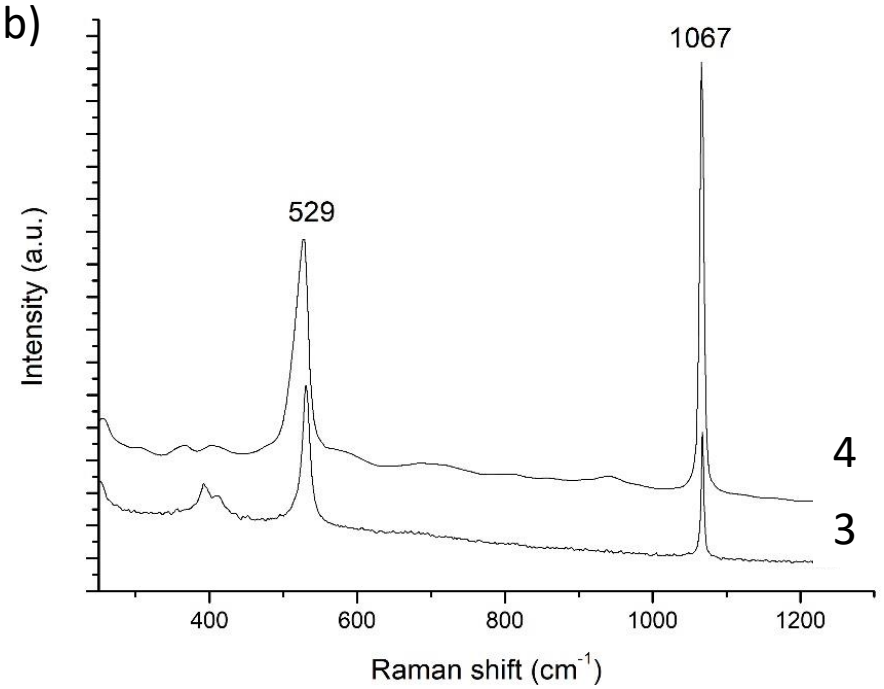
b)
Intensity (a.u.)
1067
529
4
3
400
600
800
1000
1200
Raman shift (cm-1)

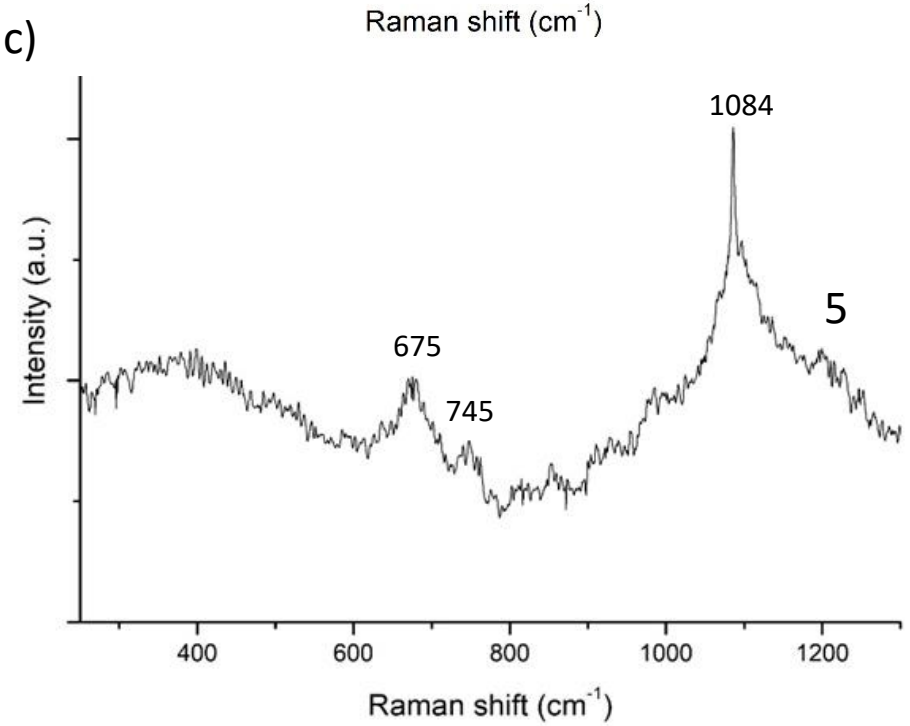
c)
Intensity (a.u.)
1084
675
745
5
400
600
800
1000
1200
Raman shift (cm-1)

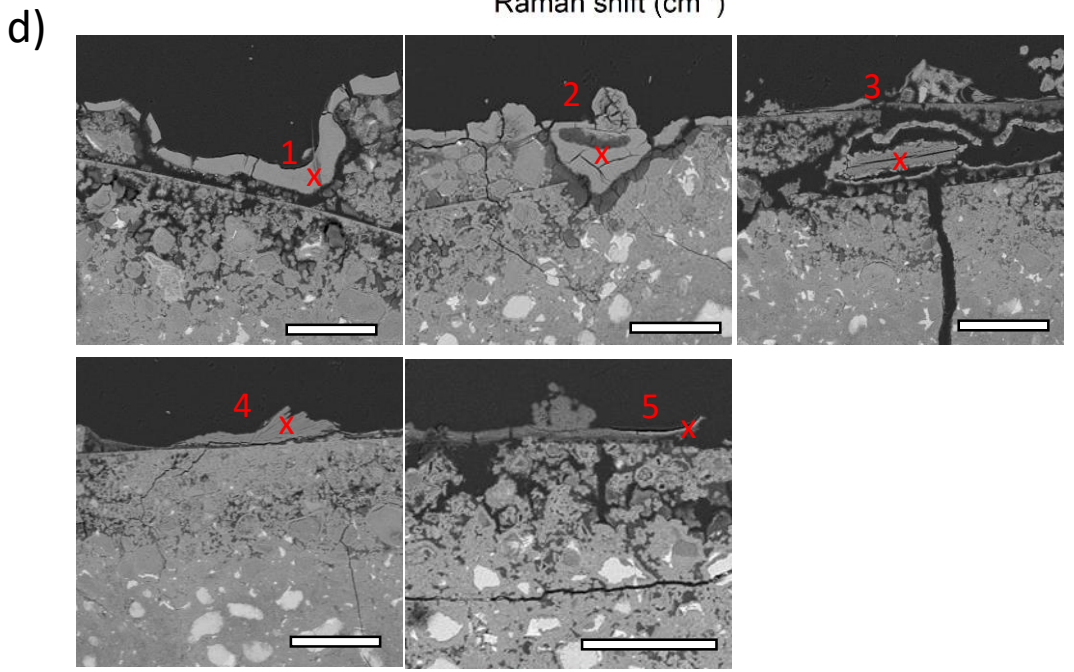
d)
1
x
2
x
3
x
4
x
5
x

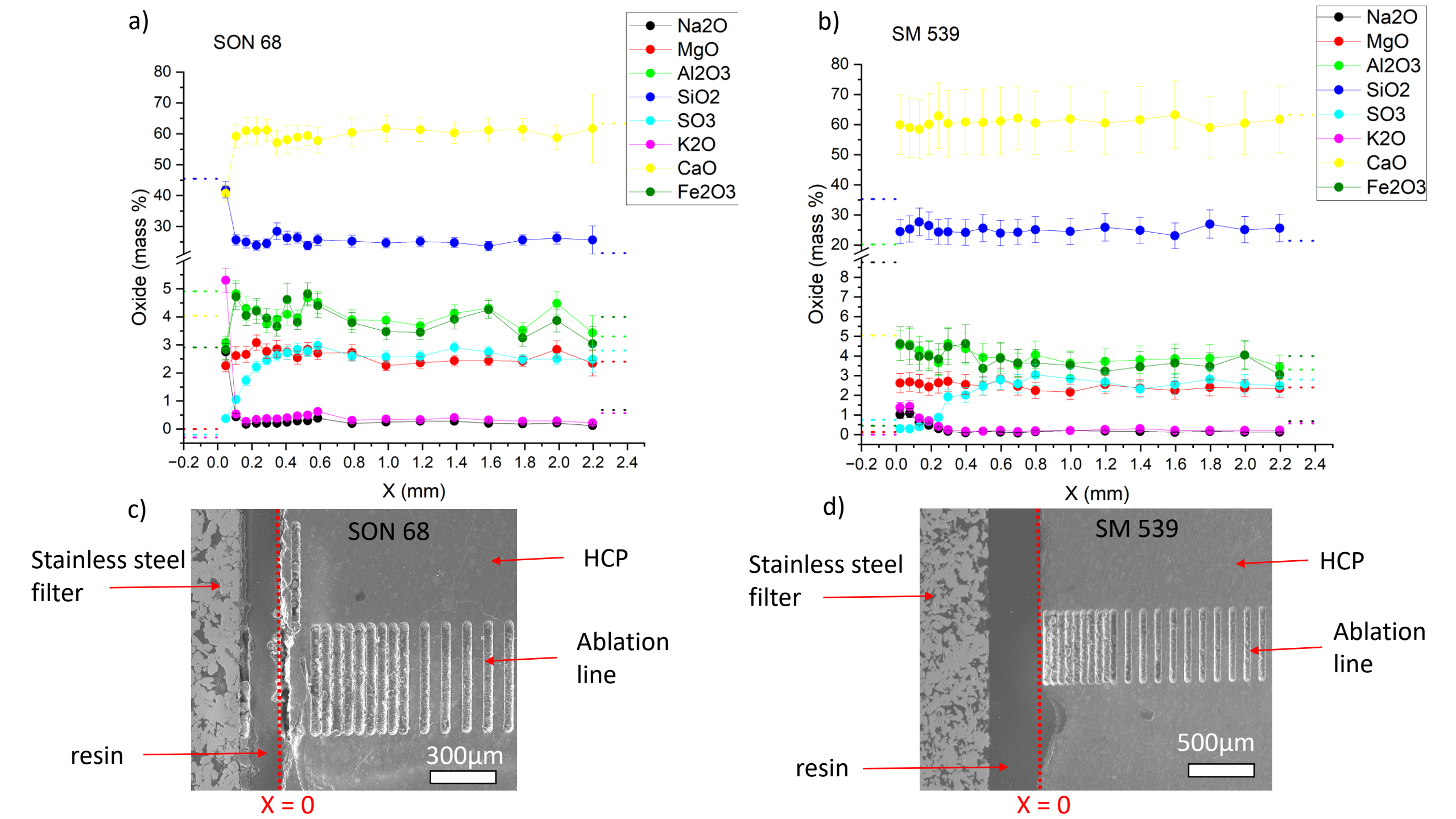
a)
SON 68
Na2O
MgO
Al2O3
SiO2
SO3
K2O
CaO
Fe2O3
Oxide (mass %)
X (mm)
b)
SM 539
Na2O
MgO
Al2O3
SiO2
SO3
K2O
CaO
Fe2O3
Oxide (mass %)
X (mm)
c)
SON 68
Stainless steel filter
HCP
Ablation line
resin
300µm
X = 0
d)
SM 539
Stainless steel filter
HCP
Ablation line
resin
500µm
X = 0

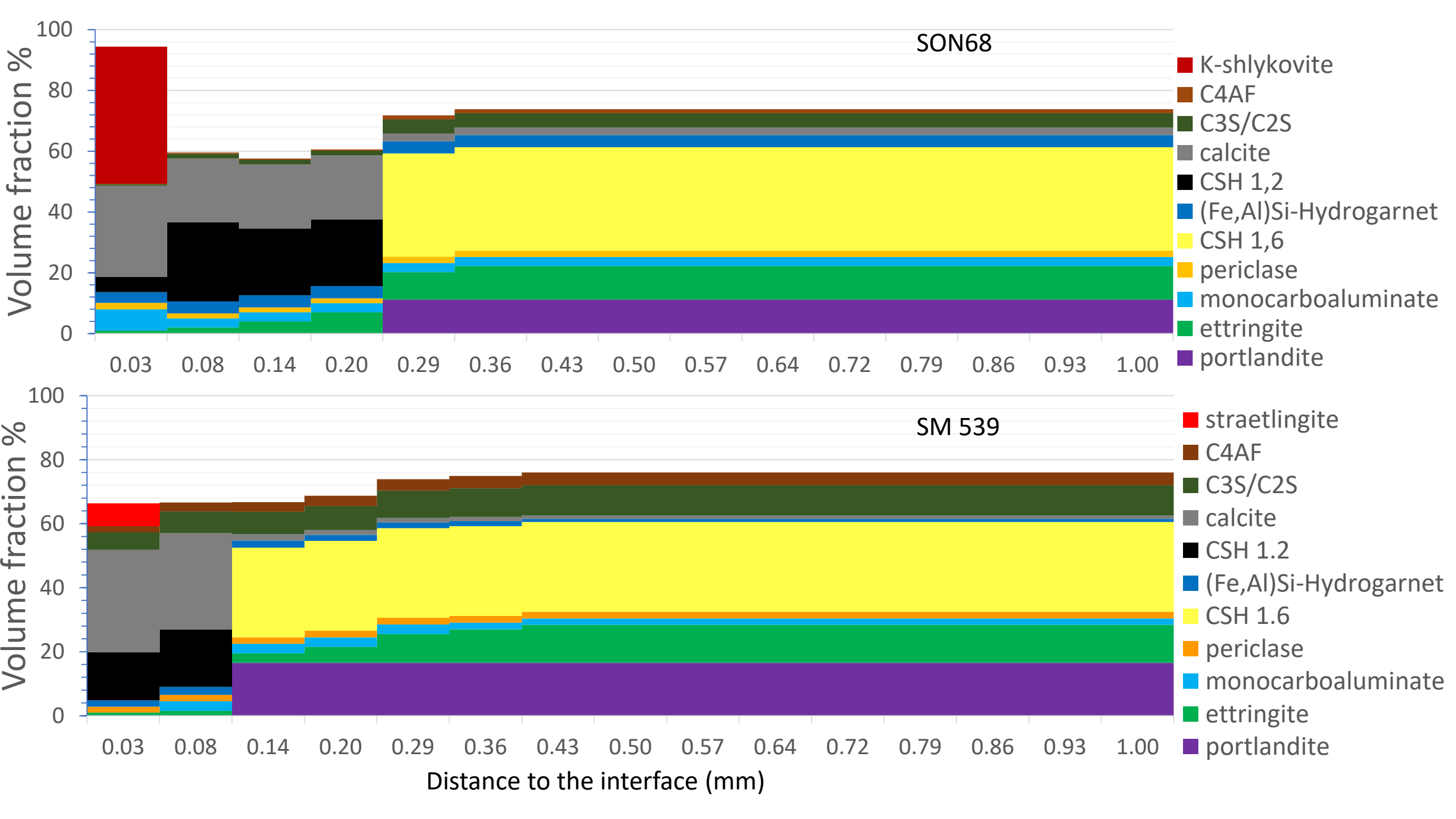
SON68
Volume fraction %
100
80
60
40
20
0
0.03
0.08
0.14
0.20
0.29
0.36
0.43
0.50
0.57
0.64
0.72
0.79
0.86
0.93
1.00
K-shlykovite
C4AF
C3S/C2S
calcite
CSH 1,2
(Fe,Al)Si-Hydrogarnet
CSH 1,6
periclase
monocarboaluminate
ettringite
portlandite
SM 539
Volume fraction %
straetlingite
C4AF
C3S/C2S
calcite
CSH 1.2
(Fe,Al)Si-Hydrogarnet
CSH 1.6
periclase
monocarboaluminate
ettringite
portlandite
Distance to the interface (mm)

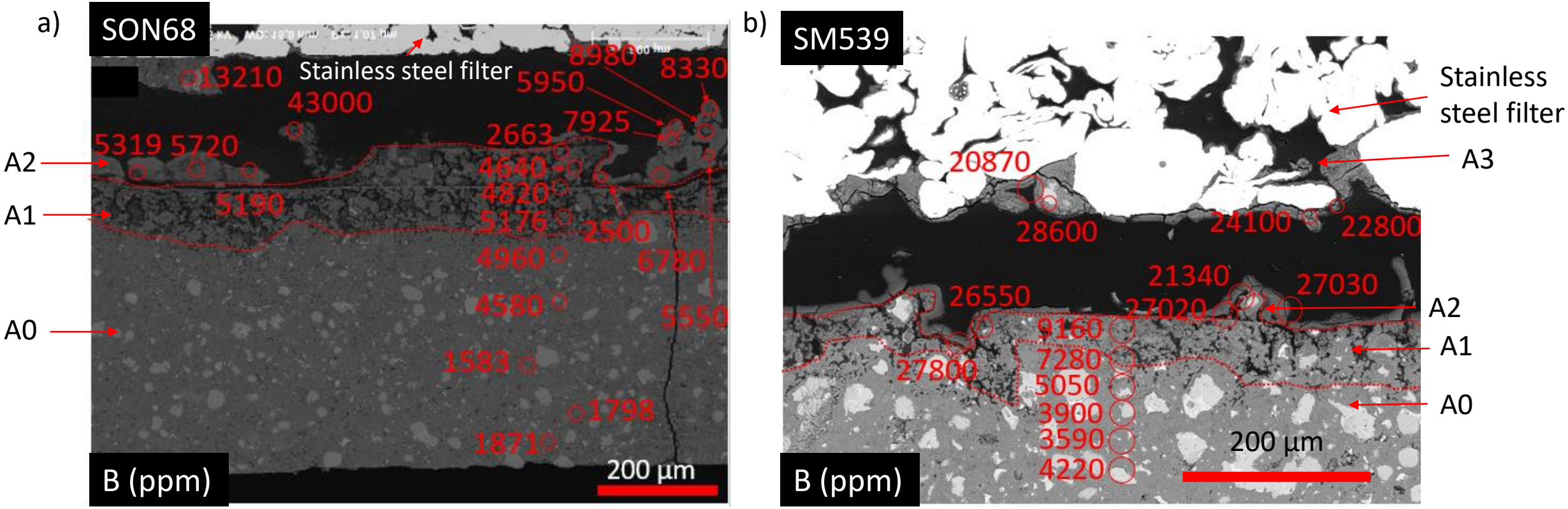
a)
SON68
Stainless steel filter
13210
43000
8980
8330
5950
7925
2663
4640
4820
5176
2500
6780
4960
4580
5550
1583
1798
1871
5319
5720
5190
A2
A1
A0
200 µm
B (ppm)
b)
SM539
Stainless steel filter
A3
20870
28600
24100
22800
21340
27030
27020
26550
27800
9160
7280
5050
3900
3590
4220
A2
A1
A0
200 µm
B (ppm)

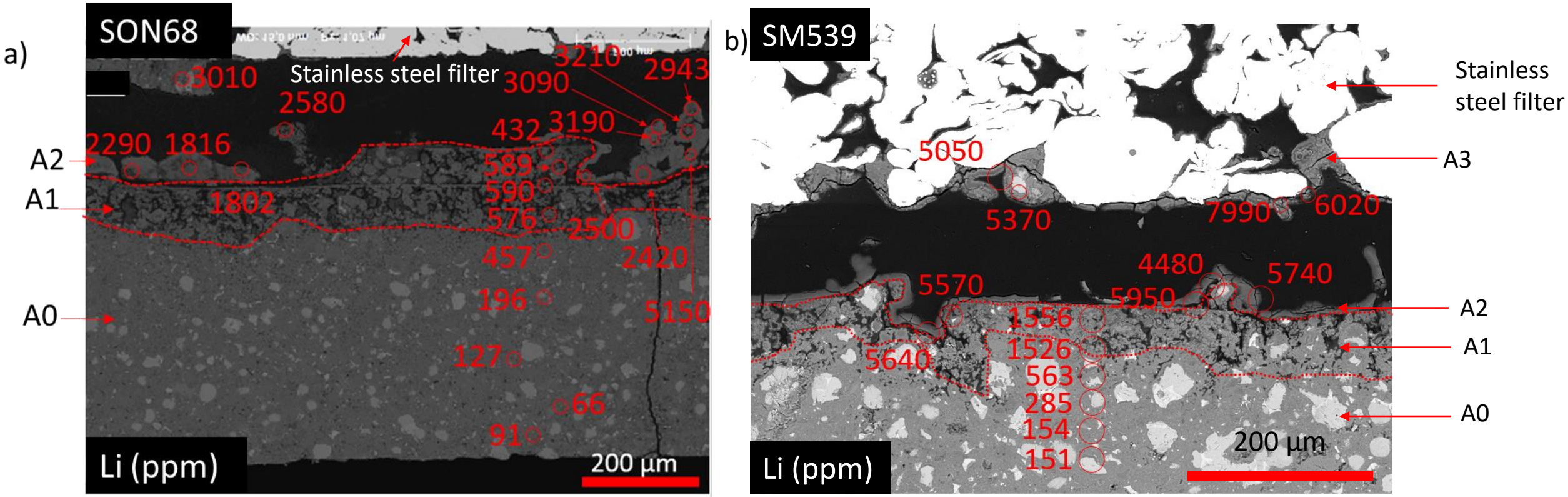
a)
SON68
Stainless steel filter
3010
2580
3210
3090
2943
3190
432
2290
1816
589
590
576
2500
1802
457
2420
196
5150
127
66
91
A2
A1
A0
Li (ppm)
200 µm
b)
SM539
Stainless steel filter
A3
5050
5370
7990
6020
4480
5740
5570
5950
1556
1526
563
285
154
151
5640
A2
A1
A0
200 µm
Li (ppm)

Oxide	SON68	SM539
SiO_2	45.48	35.27
B_2O_3	14.02	25.57
Na_2O	9.86	8.77
Al_2O_3	4.91	20.23
CaO	4.04	5.04
Li_2O	1.98	3.49
Fe_2O_3	2.91	0.45
TiO_2	0	0.003
NiO	0.74	0.011
Cr_2O_3	0.51	0.033
ZnO	2.50	0
P_2O_5	0.28	0
SrO	0.33	0.005
ZrO_2	2.65	0.046
MoO_3	1.70	0.017
MgO	0	0.130
MnO_2	0.72	0.035
CoO	0.12	0
Cs_2O	1.42	0
BaO	0.60	0
Y_2O_3	0.20	0
La_2O_3	0.90	0.007
SO_3	0	0.761

SiO_2	21.4
Al_2O_3	3.3
Fe_2O_3	4.0
CaO	63.3
MgO	2.4
SO_3	2.8
K_2O	0.57
Na_2O	0.15
Cl^-	0.03
% Na_2O eq	0.53
C3A (tricalcium aluminate)	2
Fire loss	1
Insoluble residues	0.1

Al	Ca	K	Na	Si	SO_4^{2-}	TIC	pH
$3.7x10^{-6}$	$3.45x10^{-4}$	$3.15x10^{-1}$	$1.39x10^{-1}$	$1.71x10^{-4}$	$1.91x10^{-3}$	$7.42x10^{-3}$	13.7

Phases	Formulas	Specific gravity (g/cm^3)
portlandite	$Ca(OH)_2$	2.23
CSH 1.2	$Ca_{1.2}SiO_{3.2}\cdot 2.06H_2O$	2.28
CSH 1.6	$Ca_{1.6}SiO_3.6\cdot 2.58H_2O$	2.32
ettringite	$Ca_6Al_2(SO_4)_3(OH)_{12}\cdot 26H_2O$	1.7
Fe-Si-katoite	$Ca_3Al_{0.9}Fe_{1.0}Si_{0.85}O_{12}H_{8.6}$	3.07
monocarboaluminate	$Ca_4Al_2CO_9\cdot 10.68H_2O$	2.18
C_3S/C_2S mixture	$Ca_{2.5}SiO_4$	3.25
C_4AF	$Ca_4Al_2Fe_2O_5$	3.82
calcite	$CaCO_3$	2.7
periclase	MgO	3.58
straetlingite	$Ca_2Al_2SiO_2(OH)_{10}\cdot 2.5\ H_2O$	1.97
K-shlykovite	$KCa[Si_4O_9(OH)]\cdot 3H_2O$	2.24